Check for updates

Synergistic MXene/LDH heterostructures with extensive interfacing as emerging energy conversion and storage materials

Sandhya Venkateshalu, †[a] Gracita M. Tomboc, †[ab] Suruthi Priya Nagalingam, [c] Jun Kim, [d] Tehzeeb Sawaira, [e] Kashaf Sehar, [a] Bruno G. Pollet, [b] Jin Young Kim, *[d] Andrews Nirmala Grace*[c] and Kwangyeol Lee *[a]

The heterostructures of different two-dimensional (2D) materials have garnered significant attention recently as emerging energy conversion and storage systems. Combining highly conductive and surface-active 2D MXenes with multifunctional 2D layered double hydroxides (LDHs) can leverage the constructive properties of both 2D materials. The synergistic interactions at the interface of MXene/LDH heterostructures enable them to exhibit commendable electrochemical performance and alleviate the disadvantages of the individual components. By comprehending the interfacial interactions between these two 2D materials, the structural, electronic, and morphological properties of the hybrid can be optimized. To this end, in addition to the discussions of the established synthetic methods for MXene/LDH hybrids, this article critically reviews their growth mechanism and factors influencing the morphology and chemical properties of the composites. Furthermore, the electronic interactions at the MXene/LDH heterointerface and their role in enhancing the electrochemical properties favorable to energy applications are systematically discussed. Finally, the key challenges and prospective research guidelines are provided to encourage further research to explore the synergistic effects of 2D/2D MXene/LDH hybrids in building better energy conversion and storage systems.

1. Introduction

Various two-dimensional (2D) materials with exceptional structural and electronic properties have emerged recently to spearhead innovations in the fields of electrocatalysis and energy storage systems.[1–11] Among them, MXenes and layered double hydroxides (LDHs) stand out from peer 2D materials in terms of research activities. MXenes boast high conductivity, flexible structures, hydrophilicity, and excellent mechanical stability.[12–14] On the other hand, LDHs exhibit high theoretical specific capacitance, tuneable element composition, exchangeable intercalated anions, adaptable interlayer structures, and single-layer nanosheets. However, these two materials share common problems, including severe restacking (aggregation),

poor structural/thermal/oxidative stabilities, and low durability.[15–18] Due to these shortcomings, pristine MXenes and LDHs as electrodes or electrocatalysts have not been very successful in penetrating practical applications.

Past research activities focused mostly on exploiting the intrinsic activities and the electronic properties of MXenes and LDHs, and thus the optimization of their chemical composition, surface functional groups, interfacial structure, and morphology has been the most salient research trend.[19–25] Recently, a new research venue, which explores the hybridization, regulation of surface properties, and heterointerface engineering of MXenes and LDHs, has emerged by recognizing that the properties of these two materials are rather complementary.[26–33] MXene/LDH 2D/2D heterostructures have been pursued by exploiting the different active functionalities (–O, –OH, –F, *etc.*) on the surface of MXenes and the ability of LDHs to be exfoliated into single-layer nanosheets. The electronic coupling between MXenes and LDHs at the interface of MXene/LDH heterostructures leads to improved conductivity, active sites, and stability. Charge redistribution at the heterointerface enhances mechanical and chemical stability while promoting electrochemical activity. Thus, forming 2D/2D heterostructures could alleviate the inherent shortcomings of MXene and LDH structures, such as severe restacking and volume expansion during electrochemical analysis. More importantly, MXene/LDH

[a]*Department of Chemistry and Research Institute for Natural Sciences, Korea University, Seoul 02841, Republic of Korea. E-mail: kylee1@korea.ac.kr*

[b]*Green Hydrogen Lab (GH2Lab), Institute for Hydrogen Research (IHR), Université du Québec à Trois-Rivières (UQTR), 3351 Boulevard des Forges, Trois-Rivières, Québec G9A 5H7, Canada*

[c]*Centre for Nanotechnology Research, Vellore Institute of Technology (VIT), Vellore 632014, Tamil Nadu, India. E-mail: anirmalagrace@vit.ac.in*

[d]*Hydrogen Fuel Cell Research Center, Korea Institute for Science and Technology 5, Hwarang-ro 14-gil, Seongbuk-gu, Seoul 02792, Republic of Korea. E-mail: jinykim@kist.re.kr*

[e]*School of Chemistry, University of the Punjab, Lahore 54590, Pakistan*

† These authors contributed equally to this work.

This journal is © The Royal Society of Chemistry 2023

J. Mater. Chem. A, 2023, **11**, 14469–14488 | **14469**

hybrids with weak van der Waals (vdW) interactions can preserve the individual intrinsic characteristics of each 2D layered material while exposing an immense contact interface between them, which is highly beneficial for energy storage and electrocatalysis applications. As a result of the synergy from the heterointerface, remarkable advances have appeared

in the fields of supercapacitors (hybrid, asymmetric, and all solid-state),[27,34–37] batteries (Li-ion and metal–air), electrochemical water splitting,[38–43] photocatalytic/electrochemical CO_2 reduction reaction (CO_2RR),[44–47] sensors (gas and glucose),[48,49] anti-corrosion, flame retardancy,[28] and electromagnetic wave absorbers.[50] Scheme 1 summarizes the properties, problems, and prospects of MXenes and LDHs.

Several reviews have been reported on the emerging MXene and LDH materials and their combination with various 0D, 1D, and 2D materials.[51–59] The progress of Ti_3C_2 MXene/LDH nanocomposites has also been recently summarized,

Dr Sandhya Venkateshalu received her Master's degree in Nanotechnology from Visvesvaraya Technological University, India, in 2015. Afterward, she worked as an Assistant Professor for a year at Dr T. Thimmaiah Institute of Technology, India. She received her PhD in Nanotechnology from the Vellore Institute of Technology, India, in 2021. She is currently a Research Professor at Korea University, Republic of Korea. Her research interests include the synthesis and characterization of nanomaterials, 2D nanomaterials, MXenes, and energy storage and conversion devices.

Dr Gracita M. Tomboc is working as a Research Scientist at the INM-Leibniz Institute for New Materials, Saarbrücken, Germany under the INM program division Energy Materials. She was a pioneering member of the Green Hydrogen Lab (GH₂Lab) at the Hydrogen Research Institute (HRI), University of Quebec at Trois-Rivières (UQTR) in 2022. She worked as a postdoctoral researcher at Korea University from 2019 to 2022. She holds a bachelor's degree and a professional license in Chemical Engineering, and PhD in Energy Science and Technology. Her research is mainly focused on, but not limited to the synthesis, characterization, and electrochemical measurements of novel materials for energy storage, conversion, and water catalysis technology.

Suruthi Priya Nagalingam received M.Sc. in Chemistry from the SRM Institute of Science and Technology, Kattankulathur, Tamil Nadu, India. She is currently pursuing her PhD under Prof. Dr A. Nirmala Grace at the Vellore Institute of Technology, Vellore, Tamil Nadu, India. Her research focuses on alternative Pt-free MXene based counter electrodes for DSSC applications.

Dr Jun Kim obtained his PhD degree (2020) in inorganic chemistry from Korea University and is currently working as a postdoctoral researcher at the Hydrogen Fuel Cell Research Center in the Korea Institute of Science and Technology (KIST). His current research focuses on the design of nanostructured electrocatalysts for energy conversion devices.

Tehzeeb Sawaira received her M.Phil degree in Inorganic Chemistry from the University of the Punjab, Lahore, Pakistan. She has been working as a visiting lecturer since January 2023 at Government Graduate College Zafarwal, District Narowal, Pakistan. Her research interests include photocatalytic dye degradation, synthesis of useful sensors for disease diagnosis, and synthesis of nanomaterials and nanocomposites for energy storage and conversion applications.

Kashaf Sehar has done BS (Hons.) in Chemistry at Government College University Faisalabad, Pakistan. GCUF awarded her with a gold medal for being the highest achiever of the session 2015–19. She received her Master's degree from Quaid-i-Azam University Islamabad, Pakistan in Inorganic/Analytical Chemistry in 2022, where she worked as a research assistant with Prof. Dr Amir Waseem. Her research interests are the synthesis, characterization and applications of nanomaterials, energy conversion, and energy storage.

highlighting the synthetic methods, properties, and applications of such MXene-based hybrids.[60] However, as far as we know, no critical review yet explicitly investigates the electronic interactions at the interface between these two 2D materials. A clear understanding of the origin of their synergy would establish new avenues to effectively improve their electrochemical activity, durability, and charge storage mechanism. In addition, expounding the interfacial interactions between MXenes and LDHs would simplify the design and modifications of the morphological, structural, and electronic properties of 2D/2D MXene/LDH hybrids and ultimately address their agglomeration and restacking issues. Hence, in this review, we provide a critical assessment of the synergistic interactions at the heterointerface of MXene/LDH 2D/2D heterostructures.

First, we briefly describe the fundamentals of pristine MXenes and LDHs, including the basics of their crystal structures, composition, functional groups, and established synthetic methods. Next, we discuss the important parameters/experimental conditions to successfully incorporate LDHs into the MXene structure. We indicate the difference between the facile physical attachment of LDHs into MXenes and the tight chemical interfacing of MXenes with LDHs. The effects of varying experimental parameters on the morphology and properties are elaborated in the overview of the growth mechanism of 2D/2D heterostructures. The in-depth assessment of the electronic interaction at the heterointerface of the MXene/LDH hybrid is accompanied by important characterization techniques and advanced theoretical studies to expound on how such synergistic interaction is beneficial to different energy applications. Finally, the pressing technical challenges and future research directions of the MXene/LDH hybrid are provided.

Bruno G. Pollet is a Professor of Chemistry at the Université du Québec à Trois-Rivières (UQTR), Director of the UQTR Green Hydrogen Lab, Deputy Director of the UQTR Institute for Hydrogen Research (IHR), Adjunct Professor of Renewable Energy at the Norwegian University of Science and Technology (NTNU), and member of the "NTNU Team Hydrogen". He is the President of the Green Hydrogen Division of the International Association for Hydrogen Energy (IAHE). His research covers a wide range of areas from the development of novel materials for low-temperature fuel cells and water electrolysers, hydrogen production from (non-)pure water, organics, and bio-wastes to fuel cell and electrolyser systems, demonstrators, and prototypes.

Dr Jin Young Kim obtained his PhD degree (2012) in Materials Science and Engineering from the Massachusetts Institute of Technology. After completing his postdoctoral study at the University of Toronto, he joined the Korea Institute of Science and Technology in 2013 as a research staff member. He worked at the Samsung Advanced Institute of Technology as a research staff member from 2002–2006. His current interests include the development of nanomaterials for electrochemical-based energy and environmental applications.

Professor Andrews Nirmala Grace is the Director at the Centre for Nanotechnology Research, Vellore Institute of Technology (VIT), Vellore, India. She received her PhD degree from the University of Madras, India, and worked as a Post-doctoral/Senior Researcher Fellow at the Korea Institute of Energy Research, South Korea on Renewable Energy. She is a Fellow of the Royal Society of Chemistry (FRSC) and a Fellow of the Academy of Sciences, Chennai (FASCh). Her current research interests include 2D energy materials, design and fabrication of electrodes for solar cells, and supercapacitors.

Professor Kwangyeol Lee obtained his PhD degree (1997) in Chemistry from the University of Illinois at Urbana–Champaign. After fulfilling his military obligation, he joined Korea University in 2003 as a chemistry faculty member, before being appointed as a professor. He is the recipient of the Wiley-KCS Young Scholar Award (2009, Korean Chemical Society) and the Excellent Research Award (2019, KCS Inorganic Chemistry Division). His current interests include the development of synthetic methodologies for nanoscale materials and the development of nanotechnologies to support the environment by creating sustainable energy.

This journal is © The Royal Society of Chemistry 2023

J. Mater. Chem. A, 2023, **11**, 14469–14488 | **14471**

## 2. Overview of pristine MXenes and LDHs

2.1 Structural aspects of MXenes

MXenes refer to a family of 2D transition metal carbides, nitrides, or carbonitrides.[61–63] They can be prepared *via* the selective etching of the A-layer from parent MAX phase precursors ($M_{n+1}AX_n$; $n = 1$, 2, or 3), where M stands for a transition metal (*i.e.*, Ti, V, Nb, Ta, Cr, and Mo), A is a group IIIA or IVA element, mostly aluminum (Al), and X denotes carbon and/ or nitrogen.[64–66] While the M–X bond is a mix of covalent, metallic, and ionic characters, the M–A bond is metallic only; hence, it is much weaker. The difference between the characteristics and relative strengths of M–X and M–A bonds allows the removal of the weak A-layer in the MAX precursor upon the addition of fluoride-containing acidic solutions (*i.e.*, HF and HCl + LiF) or fluoride-free alkaline solutions (*i.e.*, KOH).[67,68] A more chemically stable multi-layered MXene is then produced with a chemical formula of $M_{n+1}X_nT_x$, where T_x represents the resulting terminating surface functional groups (*i.e.*, –OH, O, and –F) and n is the number of atomic layers of the transition metal ($n = 1$ to 3; M_2X, M_3X_2, and M_4X_3). Scheme 2a illustrates the crystal structure of a pristine MXene. It possesses a hexagonal lattice structure originating from its parent MAX precursor, where M atoms are arranged in close-packed structures while X atoms occupy the octahedral interstitial sites. Notably, the arrangement of M atoms in different crystallographic structures of MXenes is fixed. For instance, in the M_2X structure, M atoms acquire hexagonal close-packed stacking mode following ABA-BAB ordering. On the other hand, in M_3X_2 and M_4X_3 structures, M atoms prefer to adopt face-centered cubic stacking mode and follow ABCABC ordering.

Double transition metal MXenes (DTM MXenes) are realized when two different metal elements (M′ and M″) replace the M layer of pristine MXenes, changing the chemical formula to $(M'M'')_{n+1}X_nT_x$.[69–74] DTM MXenes are categorized into two groups based on the metal atom arrangements within the MXene lattices: disordered (or solid-solution) DTM MXenes and
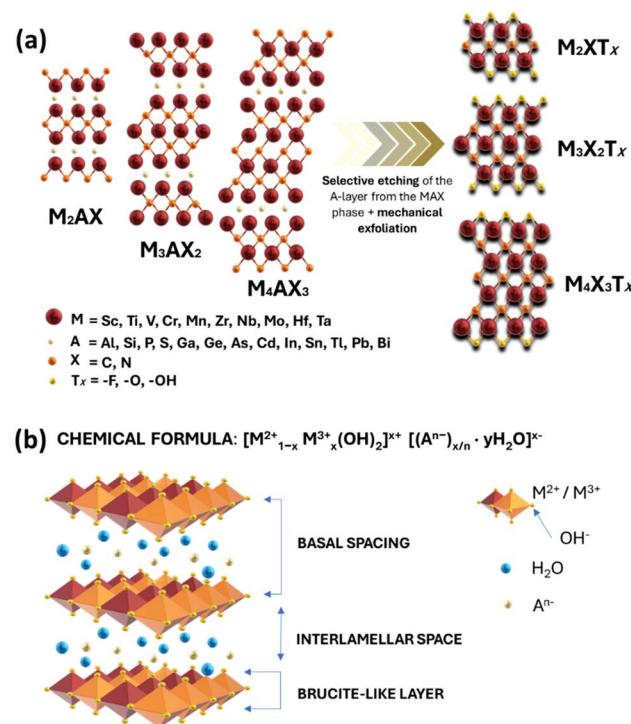
Scheme 2   Crystal structures of an (a) MXene and (b) LDH.

ordered DTM MXenes. The former type comprises two metal elements randomly arranged in the M layer without a well-defined stoichiometric constant, while the latter type possesses a non-metal atomic layer sandwiched between two distinct metal layers. The ordered-type DTM MXene is thermodynamically more stable than the solid-solution-type DTM MXenes, thus receiving more attention. By optimizing the stoichiometry of M, A, and X elements, and with the suitable selection of M′ and M″ metals, it was experimentally confirmed that two kinds of ordered DTM MXenes could be prepared from quaternary MAX phases, denoted as o-MAX and i-MAX
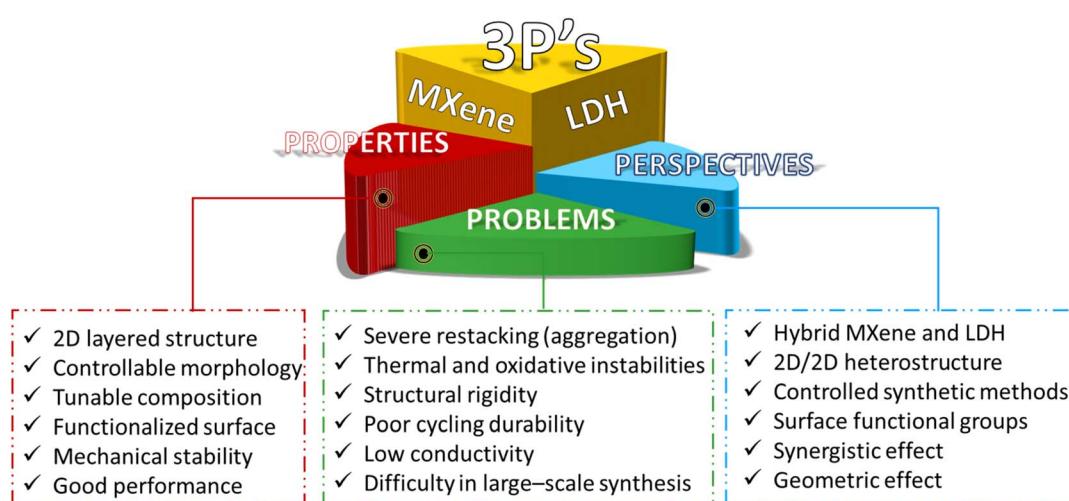
Scheme 1   Summary of the common properties, problems, and perspectives of MXenes and LDHs.

phases.[75–77] The o-MAX phases ($M'_2M''AX_3$ and $M'_2M''AX_2$) are composed of ordered out-of-plane double transition metals, with M' metal in the outer layer and M'' in the inner layer. Conversely, the M-layer of i-MAX phases is composed of two in-plane ordered double transition metals, with M' arranged in a hexagonal lattice and M'' positioned in the center of the hexagon, resulting in a 2 : 1 ratio of M' and M''. The newly discovered quaternary o-MAX and i-MAX phases are then transformed into out-of-plane ordered DTM MXenes (o-MXenes) and in-plane ordered DTM MXenes (i-MXenes), respectively, *via* finely adjusted etching conditions.[78,79]

2.2 Synthesis of MXenes

MXenes can be prepared *via* both top-down and bottom-up approaches. Top-down synthesis involves the selective etching of the A-layer from the MAX phase using aqueous HF, a mixture of an acid and fluoride salt (HF + HCl, LiF + HCl, *etc.*), molten salt mixture (KF + LiF + NaF), hydrothermal and electrochemical methods.[80–82] MXene surfaces are consequently terminated by –O, –OH, and/or –F functional groups during the etching process, which can be controlled by the etching time and temperature. The removal of the A-element *via* top-down synthesis is facile due to the weaker M–A bonds than the M–X bonds in the MAX phase, resulting in intact MXenes. 2D multi-layered MXenes are then exfoliated into a single or a few layers by chemical intercalation or mechanical dispersion. Chemical intercalation, however, drives some organic molecules to occupy the active sites of the MXene surfaces, which is likely to decrease the electrochemical activity. Although fluorine-containing solutions have been proven effective for etching the A-layer, it generates inert surfaces, which significantly affect the electrochemical properties of MXenes. Besides, fluorine-based etchants produce toxic liquid waste. For these reasons, efforts have been exerted to utilize fluorine-free solutions such as NaOH at room temperature.[83] However, present fluorine-based and fluorine-free wet etching methods result in a low yield of MXenes, particularly in high-temperature processes. Hence, for the scalable manufacturing of high-quality MXenes, it is urgent to discover a time and temperature-efficient etching procedure.

The bottom-up approaches like chemical vapor deposition (CVD), plasma-enhanced pulsed laser deposition (PEPLD), and template techniques are uncommon for MXene synthesis; hence limited research is available.[84] Halim *et al.* reported the first bottom-up approach to create a single-layer Ti_3C_2 film in 2014.[85] The group formed Ti_3AlC_2 thin films through sputter deposition and subsequently removed the Al-layer using aqueous HF or NH_4HF_2 to form Ti_3C_2 films. Xu *et al.* created a few nanometers thick ultrathin Mo_2C crystals using the CVD technique with methane and Mo foil as the carbon and Mo resources, respectively.[86] Jeon *et al.* reported the transformation of MoS_2 into a hybrid of MoS_2/Mo_2C using an epitaxial growth technique under the influence of CH_4 and H_2.[87] The main challenges of bottom-up approaches still lie in synthesizing monolayer MXene sheets with precise control over their dimensions, morphologies, surface termination, and electro-chemical characteristics.

In addition to the aforementioned widely employed methods for synthesizing MXenes, there exist several other notable techniques such as algae extraction, alkali etching, UV-induced etching, Lewis acid molten salt etching, halogen etching, magnetron sputtering, ion beam sputtering, and ammoniation.[88–95] These newly reported alternative approaches have shown promise in producing MXenes with unique properties, expanding their application range.

2.3 Structural aspects of LDHs

Metal hydroxides ($M(OH)_2$, M = Co^{2+}, Ni^2, Zn^{2+}) are compounds having a layered hexagonal structure and exist in two poly-morphic forms: α and β.[96–99] The α-form is hydroxyl-deficient and consists of positively charged layers of $M(OH)_{2-x}\cdot(H_2O)_x$ and is isostructural with LDH compounds. On the other hand, the β-form is a stoichiometric phase of $M(OH)_2$ and is iso-structural to brucite mineral $Mg(OH)_2$, which is a typical example of the LDH material. In this context, it is necessary to clearly define the basic structural features of LDHs to differen-tiate them from ordinary metal hydroxides with a layered structure. Note that if only divalent cations are involved in the layer, such as that of β-phase metal hydroxides, the layer is usually neutral and does not require compensating anions. However, if the divalent metal cations in the layer are either replaced with trivalent cations or oxidized to a trivalent state, the layer becomes positively charged. In this case, intercalating anions are necessary to neutralize the charge of the layer. Such anion intercalation distinguishes LDHs from ordinary layered metal hydroxides.

Scheme 2b illustrates the typical layered and galleried structure of a LDH, consisting of positively charged hydroxide layers with anions and water molecules intercalated between layers.[100] The general formula of the LDH structure is $(M_{1-x}^{2+}M_x^{3+}(OH)_2)(A_{x/n}^{n-}\cdot nH_2O)$, where M^{2+} (*i.e.*, Ca^{2+}, Mg^{2+}, Zn^{2+}, Ni^{2+}, Mn^{2+}, Co^{2+}, and Fe^{2+}) and M^{3+} (Al^{3+}, Cr^{3+}, Mn^{3+}, Fe^{3+}, Ga^{3+}, Co^{3+}, and Ni^{3+}) are the respective divalent and trivalent metal cations located in the brucite-like host layers. A^{n-} (CO_3^{2-}, $NO_3^{\cdot-}$, SO_4^{2-}, F^-, $ClO_4^{\cdot-}$, and PO_4^{3-}) is the charge-compensating anion in the interlayer region, and X is the molar ratio of the trivalent metal ions relative to the sum of the trivalent and divalent metal ions (usually $0.2 < X < 0.33$).[101–103] The metal cations of LDHs have similar ionic radii and are coordinated by six oxygen atoms forming $M^{2+}/M^{3+}(OH)_6$ octahedra. These octahedra form two-dimensional sheets *via* edge sharing and may stack together by hydrogen bonding between the hydroxyl groups of adjacent sheets. The interlayer guest anion has a negative charge and plays a decisive role in the construction and functional regula-tion of the host and guest functional materials.

2.4 Synthesis of LDHs

Several comprehensive reviews about the detailed synthesis of LDHs are available; hence, we briefly describe the primary methods to prepare pristine LDHs.[104–108] The synthetic methods could primarily be grouped into direct and indirect methods.

Coprecipitation, electrochemical, hydrothermal, salt oxide, and sol–gel processes are the main strategies for direct synthesis, while post-treatments such as anion exchange, reconstruction, and delamination are known indirect synthetic methods.[60,108]

On the one hand, the coprecipitation process is one of the most efficient methods for the large-scale production of LDHs in powder form.[108] In a typical experiment, NaOH, NH$_4$OH, Na$_2$CO$_3$, or NaHCO$_3$ solution is added dropwise to the aqueous solution containing divalent and trivalent metal salts at room temperature. The metal ions are coprecipitated in the alkaline solution under constant stirring to produce LDHs. The pH of the reaction medium is maintained constant within the range of 7 to 11, depending on the composition of the metal ions. The

slurry with the LDH precipitate is heated for a few hours to improve the crystallinity. On the other hand, *in situ* growth is the most effective and extensively used direct approach for coating LDHs on a metal substrate.[109]

The hydrothermal process is a simple technique to produce homogeneous LDHs by treating two or more metal oxides in an aqueous solution with targeted anions at a high temperature and pressure.[110] The sol–gel method, a mild synthetic route, can produce high-quality uniform LDH nanoparticles and thin films.[111] The LDH prepared using the sol–gel method is purer with a higher specific surface area than the LDH obtained through coprecipitation; however, the sol–gel method results in LDHs with low crystallinity. The anion exchange process is an indirect
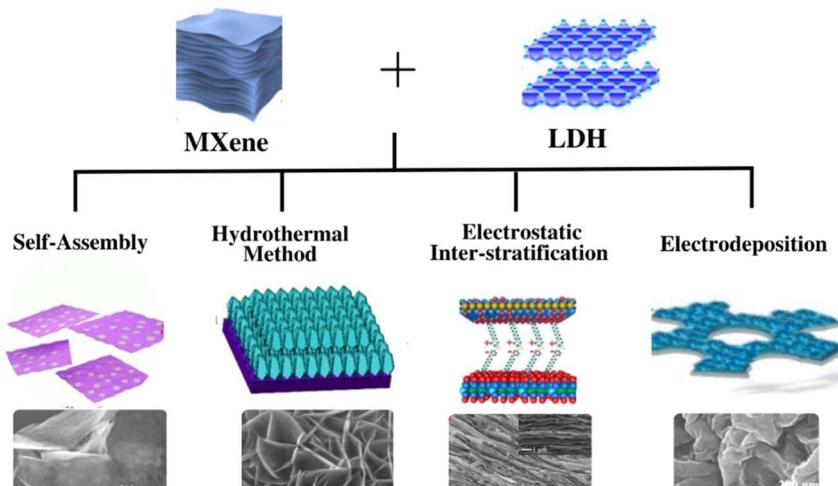

Fig. 1 Summary of the methods used to synthesize MXene/LDH nanocomposites. Reproduced with permission from ref. 119 copyright 2021, Elsevier. Reproduced with permission from ref. 26 copyright 2019, Elsevier. Reproduced with permission from ref. 128 copyright 2019, Elsevier. Reproduced with permission from ref. 135 copyright 2020, Elsevier.
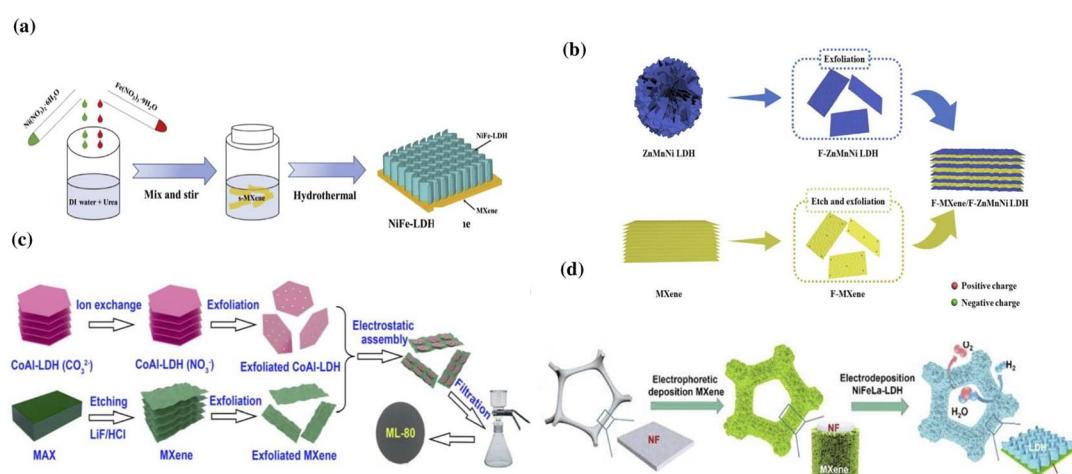
Fig. 2 (a) Schematic representing the synthesis of a NiFe–LDH/MXene composite using the hydrothermal method. Reproduced with permission from ref. 30 copyright 2020, Elsevier. (b) Self-assembly of the F-MXene/F−ZnMnNi LDH. Reproduced with permission from ref. 120 copyright 2020, American Chemical Society. (c) Electrostatic assembly of the MXene/CoAl-LDH hybrid. Reproduced with permission from ref. 33 copyright 2019, Elsevier. (d) Fabrication of NiFeLa-LDH/v-MXene/NF through electrodeposition. Reproduced with permission from ref. 41 copyright 2022, Elsevier.

14474 | *J. Mater. Chem. A*, 2023, **11**, 14469–14488

This journal is © The Royal Society of Chemistry 2023

synthesis method to modify the anions in the interlayer region of the pre-synthesized LDH.[112] Since an LDH precursor is required, the anion exchange method technically cannot be considered a true synthesis technique but rather a modification step. Typically, excess salts of the desired anions are stirred with the aqueous suspension of pre-synthesized LDHs to modify the interlayer anions. LDHs containing inorganic or organic anions can be effectively prepared using this approach.

3. Synthesis and growth mechanism of MXene/LDH hybrids

As described earlier, the synergistic effects arising from the hybridization of the two 2D materials, MXenes and LDHs, could help overcome the limitation of the pristine materials and utilize the individual benefits to enhance the electrochemical performance. The detailed synthesis and growth mechanism of MXene/LDH hybrids are described in the following sections.

3.1 Synthetic methods

Various methods have been employed to produce nanocomposites comprising evenly distributed LDHs on the surface of MXenes. Every synthetic method has its advantages and results in MXene/LDH hybrids with a unique morphology, as shown in Fig. 1. The most commonly used methods to produce MXene/LDH hybrids are discussed in this section.

3.1.1 Hydrothermal method. In a hydrothermal technique, the powders are dissolved and recrystallized using water as the solvent in a hermetically sealed pressure vessel.[113] The hydrothermal process is a simple and preferred nanoparticle synthesis method due to its low energy consumption, high crystallinity of the products, low environmental hazards, and effective dispersion. Furthermore, hydrothermal synthesis also requires less expensive instruments, precursor chemicals, and lower energy than solid and gas-phase techniques. When used in the synthesis of MXene heterostructures, the hydrothermal method enhances the activity of the MXene and alters its surface functional groups at high pressure and temperature.[114]

The hydrothermal method is widely used in the production of MXene/LDH hybrids as it aids in tuning the structure and composition of the composite by varying the temperature and reaction time.[54,114–116] For example, Zhou et al. reported a uniform growth of NiFe-LDH on $Ti_3C_2T_x$ using the hydrothermal method.[30] In a typical synthesis process, multi-layered $Ti_3C_2T_x$ was prepared by etching 1 g of Ti_3AlC_2 with 10 mL of hydrofluoric acid and converting it to a single-layered MXene by delaminating with dimethyl sulfoxide (DMSO). NiFe-LDH was synthesized by sonicating equal amounts of iron nitrate and nickel nitrate along with urea and deionized water for 10 min. The as-prepared LDH was added to the MXene and stirred for 30 minutes, and then heated to 120 °C for 18 h in a Teflon kettle to obtain a NiFe-LDH/$Ti_3C_2T_x$ hybrid. The schematic representing the formation of NiFe-LDH/$Ti_3C_2T_x$ through the hydrothermal method is shown in Fig. 2a. The peak shift in the X-ray diffraction (XRD) pattern of the nanocomposite indicated an increase in the interstitial spaces from 1.38 nm to 1.57 nm,

demonstrating that the addition of NiFe-LDH successfully prevented the restacking of MXene sheets. Li et al. reported the lateral formation of NiCo-LDH at the interface of $Ti_3C_2T_x$ using a hydrothermal method, which resulted in a hybrid $Ti_3C_2T_x$/NiCo-LDH with a 3D porous morphology.[26] Transmission electron microscopy (TEM) confirmed the porous complex network, and energy dispersive X-ray spectroscopy (EDX) analysis indicated the presence of evenly distributed Co, Ni, Ti, O, and C components in the $Ti_3C_2T_x$/NiCo-LDH hybrid. The presence of $Ti_3C_2T_x$ altered the morphology of NiCo-LDH, and the 3D interlinked porous networks in the hybrid enabled enhanced electrolyte penetration and interaction with the components of the hybrid. Likewise, in the hydrothermally synthesized V_2CT_x/NiV-LDH hybrid with uniformly coated NiV-LDH on the surface of V_2CT_x, the V_2CT_x not only prevented the aggregation of NiV-LDH sheets but also relieved the volume change, significantly improving the electrical conductivity and increasing the number of active sites.[117]

3.1.2 *In situ* self-assembly. The *in situ* synthesis is a simple and cost-effective technique to obtain MXene/LDH hybrids. The LDH grows *in situ* on the abundant heterogeneous nucleation sites on the negatively charged MXene sheets. The functional groups on the surface of the MXene enhance the synergy between the two reacting components, allowing faster charge transportation and a higher ion dispersion rate between the LDH and MXene than the mechanically mixed MXene/LDH.[26,118] The *in situ* assembled LDH in the MXene/LDH hybrid has reduced size, usually measuring less than 10 nm.[119] The *in situ* synthesis method produces hybrids with enhanced structural, electrical, and chemical features.[54] Sun et al. reported the synthesis of exfoliated ZnMnNi LDH and exfoliated $Ti_3C_2T_x$ MXene (F–ZnMnNi LDH/F-MXene) heterostructures using self-assembly.[120] The attraction between the negatively charged F-MXene and the positively charged F–ZnMnNi LDH enabled them to self-assemble after stirring the solution mixtures for 24 h. The moisture in the solution was removed by freeze-drying. The schematic representing the *in situ* assembly of F–ZnMnNi LDH/F-MXene is shown in Fig. 2b. Feng et al. reported that the MXene/LDH hybrid synthesized by an *in situ* self-assembly method exhibited a very high surface area due to its special layered micro-morphology.[121] Similarly, the V_2CT_x MXene/NiV LDH synthesized *in situ* had high electrical conductivity with abundant holes and channels, facilitating electrolyte diffusion.[117] Wang et al. reported the *in situ* vertical growth of NiCo-LDH nanosheets on $Ti_3C_2T_x$.[122] The OH^- groups on the MXene adsorbed Ni^{2+} and Co^{2+} ions, which were reduced by $NaBH_4$ solution, to form the hybrid. The vertically grown NiCo-LDH on both sides of the MXene formed a sandwich-like structure, preventing the aggregation of NiCo-LDH and the oxidation of the MXene.

3.1.3 Electrostatic interstratification. In the process of *in situ* self-assembly, various atomic interactions such as hydrogen bonding, capillary, hydrophobic forces, and van der Waals forces play a significant role in facilitating the spontaneous grouping of molecules.[123] These interactions can potentially lead to the formation of coordination bonds in certain cases.[124] However, electrostatic interstratification differs in nature, as it

This journal is © The Royal Society of Chemistry 2023

J. Mater. Chem. A, 2023, 11, 14469–14488 | 14475

involves the attraction between opposite charges without the actual formation of primary bonds.[125] Consequently, electrostatic interstratification represents a modified form of self-assembly, where two nanostructures with opposing charges come together in an aqueous environment.

Electrostatic interstratification is a simple method where the thickness of the resulting nanostructure could be effectively tuned.[126] This is a widely used method to produce 2D heterojunctions and a wide range of MXene-based heterostructures. The 2D nanostructures with multiple functional features can be restacked into heterostructures *via* electrostatic intercalation, incorporating the undeniable unique properties of each constituent.[114,127] The electrostatic attraction between the positively charged LDH and the negatively charged MXenes enables them to assemble into interlayered structures.[128] The electrostatically adsorbed cations and anions in the hybrid assembly prevent the restacking of their counterparts. Feng *et al.* reported that the anion–cation electrostatic attraction aided by the ultrasonic dispersion enabled the interlayered assembly of a $Ti_3C_2T_x$/NiCo-LDH hybrid.[127] Scanning electron microscopy (SEM) and TEM analysis indicated the alternating stacking of the MXene and LDH with a distance of 1.62 nm between the two materials. Niu *et al.* reported the electrostatic face-to-face assembly of $Ti_3C_2T_x$/CoAl-LDH at the molecular level resulting in a 3D freestanding film with a thickness of 13 mm.[33] As shown in Fig. 2c, the hybrid was prepared by gradually adding CoAl-

LDH to an MXene solution while stirring it in an ice-water bath under Ar for 60 min. The mixture was sonicated and then vacuum filtered through a porous polypropylene membrane to create a freestanding film, which was then baked in a vacuum oven overnight. Zhang *et al.* reported a simultaneous doping-electrostatic synergic assembly to fabricate a nanoflower-like Co-doped NiMn-LDH/V_2CT_x MXene.[129] The V_2CT_x MXene acted as a substrate and improved the conductivity, while the Co-doped NiMn-LDH increased the electrochemical activity and prevented the aggregation of the sheets.

3.1.4 Electrodeposition. Electrodeposition (ED) is a simple and efficient synthesis method for mass production.[130,131] ED refers to the selective distribution of material on the surface of a conducting substance by using electrical current from an ionic species-containing solution.[132] The use of a high magnetic field along with an electric field in the deposition process is called magneto-electrodeposition, which not only resolves the slow movement of mass during the ED but also manipulates the tiny structures of the electrode material, hence playing an important role in the enhancement of the electrochemical performance of the material.[133] The applied high magnetic field can decrease the size of the diffusion layer and speed up the mass movement during the ED.[134] Most reports on the synthesis of MXene/LDH hybrids through ED follow a two-step process wherein the MXene is initially deposited onto a substrate such as nickel foam, and the LDH is subsequently deposited on the MXene/
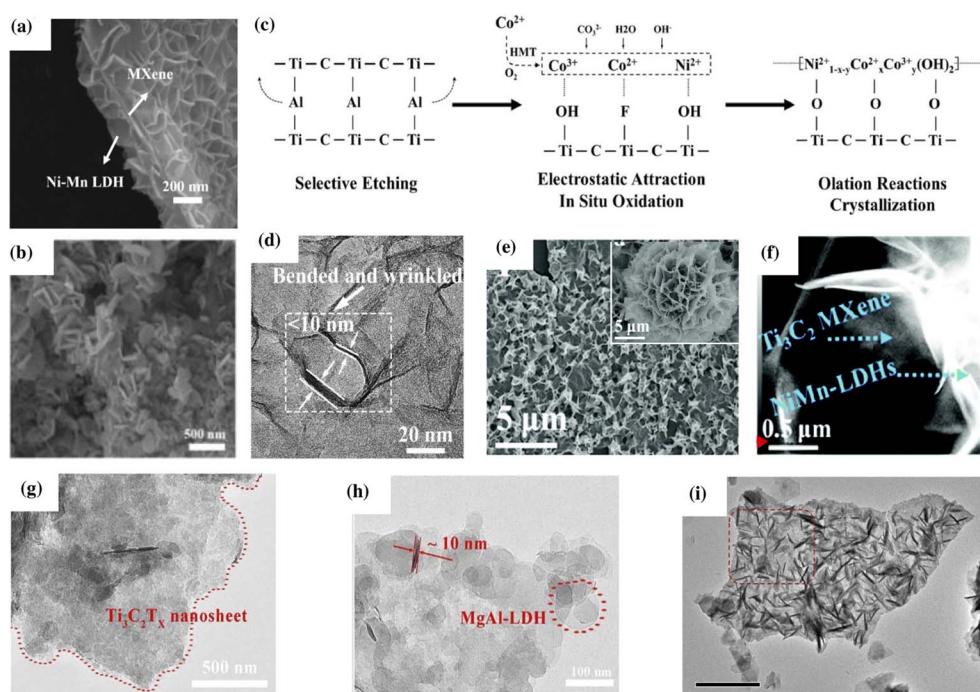
Fig. 3 (a) SEM image of MXene@Ni–Mn LDH depicting a sandwich like-morphology. Reproduced with permission from ref. 37 copyright 2020, Elsevier. (b) SEM image of 3D interconnected Fe_1Ni_3-LDH/Ti3C_2T_x-MXene nanohybrids. Reproduced with permission from ref. 138 copyright 2021, Elsevier. (c) Reaction mechanism and (d) TEM image of NiCo-LDH/Ti_3C_2 sheets. Reproduced with permission from ref. 139 copyright 2020, Elsevier. (e) SEM image depicting the nanoflower morphology of NiMn-LDHs (inset) and NiMn-LDHs/Ti_3C_2-MXene hybrids and (f) high-angle annular dark-field scanning transmission electron microscopy (HAADF-STEM) image of the NiMn-LDHs/Ti_3C_2 hybrid (ref. 140). (g and h) TEM images of $Ti_3C_2T_x$ MXene@MgAl-LDH. Reproduced with permission from ref. 119 copyright 2021, Elsevier. (i) TEM image showing the vertical growth of CoFe-LDH on the MXene. Reproduced with permission from ref. 118 copyright 2019, Elsevier.

14476 | *J. Mater. Chem. A*, 2023, **11**, 14469–14488

This journal is © The Royal Society of Chemistry 2023

substrate.[41,135,136] Yu et al. reported the ED of La-doped NiFe-LDH nanosheets on an electrophoretically deposited 3D vertically aligned $Ti_3C_2T_x$ MXene on nickel foam substrates (v-MXene/NF) (Fig. 2d).[41] The electrophoretically deposited v-MXene/NF, Pt foil, and Ag/AgCl were used as the respective working, counter, and reference electrodes. The electrolyte consisted of a combination of hydrated nitrates of Fe, Ni, and La with a molar ratio of 0.5 : 1 : 0.5. A voltage of -1.0 V was applied during the 300 s potentiostat depositing phase. Various electrodes were prepared by varying the deposition duration and the ratios of Ni/Fe/La salts in the electrolyte. The absence of NiFeLa-LDH peaks in the XRD pattern of NiFeLa-LDH/v-MXene/NF suggests that the amorphous sheets of NiFeLa-LDH deposited on the MXene surface provide defective sites for enhancing the electrocatalysis.

Similarly, CoNi LDH/$Ti_3C_2T_x$/NF was synthesized by ED using Co^{2+} and Ni^{2+} solutions, and the $Ti_3C_2T_x$/NF electrode exhibited excellent catalytic activity.[135] The –F and –OH terminal groups of $Ti_3C_2T_x$ significantly increased the activity of pure CoNi-LDH when electrically coupled. The electrodeposited CoNi-LDH/$Ti_3C_2T_x$ had excellent activity, efficient kinetics, and excellent stability toward electrocatalysis. Moreover, a self-standing ultrathin MXene/LDH hybrid on a conductive substrate could be successfully synthesized using ED, resulting in a binder-free electrode with high conductivity.[136] Li et al. reported the use of high magnetic fields (up to 9 T) during electrodeposition to fabricate NiCo-LDH and $Ti_3C_2T_x$ functionalized on carbon cloth.[137] Magneto–electric field interaction during the magneto-electrodeposition increases the mass loading and active site accessibility through the magneto-hydrodynamic effect. Moreover, the direction of the magnetic field with respect to the electric field controls the morphology of the resulting hybrid.

3.2 Formation mechanism

Depending on the type of synthesis method, experimental conditions, and the composition of the MXene and LDH, the MXene/LDH hybrid follows different formation mechanisms and exhibits different morphologies. It was reported that even the same synthesis technique could result in different morphologies. For example, the in situ assembly method can lead to a face-to-face assembly of the MXene and LDH, vertical growth of the LDH on the MXene, or can form 3D interconnected porous networks.[118,138] By adjusting the synthetic conditions, the morphology and properties of the hybrid could be effectively tuned. This section discusses the various factors influencing the formation mechanism and morphology of the hybrid.

Wang et al. designed a new NiMn LDH–MXene–LDH hybrid with a sandwich like-morphology via the coprecipitation method.[37] The morphology of vertical NiMn LDHs enveloping the top and bottom surfaces of Ti_3C_2 MXene was investigated using SEM (Fig. 3a). The 4 h reaction time yielded more NiMn LDH nanoplates than the 2 h reaction and produced 3D multi-aperture homogeneous nanostructures. As the reaction time extended, the surface of the MXene nanosheets was completely coated with NiMn LDH nanoplates, diminishing the pre-formed

open structures. Likewise, Zhang et al. reported the in situ synthesis of FeNi-LDH arrays anchored on $Ti_3C_2T_x$ using a three-step process involving an etching reaction, detachment procedure, and hydrothermal growth.[138] Different ratios of Fe and Ni in the LDH resulted in different structures. Specifically, 3D interconnected hierarchical Fe_1Ni_3-LDH arrays, evenly distributed throughout the few-layer $Ti_3C_2T_x$ flakes, were created after the hydrothermal treatment (Fig. 3b).

Zhang et al. reported a detailed reaction mechanism of NiCo-LDH on the Ti_3C_2 surface (Fig. 3c).[139] Pristine NiCo-LDH formed from crystallization and olation reactions between Co^{3+}, Ni^{2+}, and unoxidized $Co(OH)_2$ displayed a nanoflower morphology. The positive Co and Ni ions were electrostatically attracted to the negative Ti_3C_2, resulting in the in situ growth of NiCo-LDH on the MXene surface under hydrothermal conditions. However, due to the strong interaction forces between the two 2D materials, the generation of the β-phase crystal of NiCo-LDH is inhibited. Such inhibition generated ultra-thin, bent, and wrinkled NiCo-LDH nanosheets on Ti_3C_2 MXene with an interlayer spacing of ≈ 8.1 Å (Fig. 3d). The group also elaborated on the effect of different ratios of Ti_3C_2 on the morphology of NiCo-LDH/Ti_3C_2. It was observed that the hybrid retained the same morphology regardless of the amount of Ti_3C_2. Thus, they proposed that the surface confinement approach can be applied to any 2D material with negative surface charges. Similarly, Liu et al. deposited thin layers of NiMn-LDHs on the Ti_3C_2 MXene surface via a facile hydrothermal method.[140] NiMn-LDHs initially exhibited a flower-shaped morphology (Fig. 3e); however, upon in situ growth on the surface of Ti_3C_2 nanosheets, their morphology evolved to a stacked sheet structure, forming a 2D/2D hybrid structure (Fig. 3f).

Hu et al. reported the electrodeposition of CoNi-LDH on pre-synthesized $Ti_3C_2T_x$-NF to form a CoNi-LDH/$Ti_3C_2T_x$-NF hybrid.[135] The electrodeposition was carried out by immersing $Ti_3C_2T_x$-NF into a solution containing Co^{2+} and Ni^{2+} ions. Upon applying a suitable potential, CoNi LDH was tightly bound to the surface of the MXene due to the presence of distinct terminal groups –OH and –F. CoNi LDH and $Ti_3C_2T_x$ MXene interacted strongly at the interface, resulting in exceptional electronic coupling. Cai et al. reported the electrostatic adsorption of Mg^{2+} and Al^{3+} on the negatively charged $Ti_3C_2T_x$ followed by in situ nucleation and growth under hydrothermal conditions to form a $Ti_3C_2T_x$@MgAl-LDH heterostructure with face-to-face assembly.[119] TEM analysis indicated that the lamellar $Ti_3C_2T_x$ measuring several microns offered numerous active sites for the adsorption of Mg^{2+} and Al^{3+} and promoted the nucleation of MgAl-LDH (Fig. 3g and h).

Hao et al. reported the in situ 3D vertical growth of CoFe-LDH on $Ti_3C_2T_x$.[118] The –OH and –F functionalized MXene nanoflakes with surface energies >250 mJ m^{-2} stabilize the system by adsorbing metal ions. CoFe LDH tends to form clusters and stack on the MXene during MO_6 hydrolysis and olation (i.e., Co and Fe units).[141] However, due to the strong electrostatic repulsion between the newly grown CoFe LDH and as-formed LDH/MXene hybrid, the subsequent LDH was forced to grow vertically on the substrate, generating a "house of cards" structure. The –OH and –F functionalized MXene nanoflakes

This journal is © The Royal Society of Chemistry 2023

J. Mater. Chem. A, 2023, **11**, 14469–14488 | **14477**

Table 1 Morphology-based classification of the MXene/LDH hybrids for different applications

Nanohybrids	Synthesis method	Morphology	Application	Ref.
V_2CT_x/NiV-LDH	Hydrothermal	3D interconnected porous network	Supercapacitor	117
NiCo-LDH/$Ti_3C_2T_x$	Magneto-electrodeposition	3D cross-linked nest-like	Supercapacitor	137
NiCoAl-LDH/V_4C_3	Hydrothermal	3D interconnected porous network	Supercapacitor	145
$Ti_3C_2T_x$/CoNi-LDH	Electrostatic deposition	3D interconnected porous network	Supercapacitor	143
FeNi-LDH/$Ti_3C_2T_x$	Hydrothermal	3D interconnected porous network	Supercapacitor	138
CoAl-LDH/$Ti_3C_2T_x$	Electrostatic assembly	Face-to-face heterostructure	Supercapacitor	33
CoFe-LDH/$Ti_3C_2T_x$	In situ growth	House of cards	OER	118
CoFe-LDH/$Ti_3C_2T_x$	Electrostatic assembly	House of cards	OER	144
NiMn-LDH/$Ti_3C_2T_x$	Hydrothermal	House of cards	OER	140
NiCo-LDH/$Ti_3C_2T_x$/NF	Hydrothermal	House of cards	OER	43
NiAl-LDH/$Ti_3C_2T_x$	Hydrothermal	Core–shell	Photocatalytic CO_2 reduction	44

with surface energies >250 mJ m^{-2} stabilized the system by adsorbing metal ions. Notably, intercalated carbonate anions formed during the breakdown of urea assisted the vertical growth of LDH nanoarrays by preventing plane formation in the (001) direction.[142] Fig. 3i shows the TEM images of CoFe-LDH/MXene from the vertical development of the LDH on the MXene.

The morphology of the MXene/LDH hybrid plays a significant role in determining their properties. Tuning the morphology of the hybrid according to the application is indispensable to achieving high performance. By analyzing the hitherto reports on MXene/LDH hybrids, we identified the existence of appropriate morphology-application pairs. A morphology-based classification of the hybrids is given in Table 1. The optimal morphology of the MXene/LDH heterostructure for energy storage applications appears to be a 3D interconnected porous network or a face-to-face assembly. On the
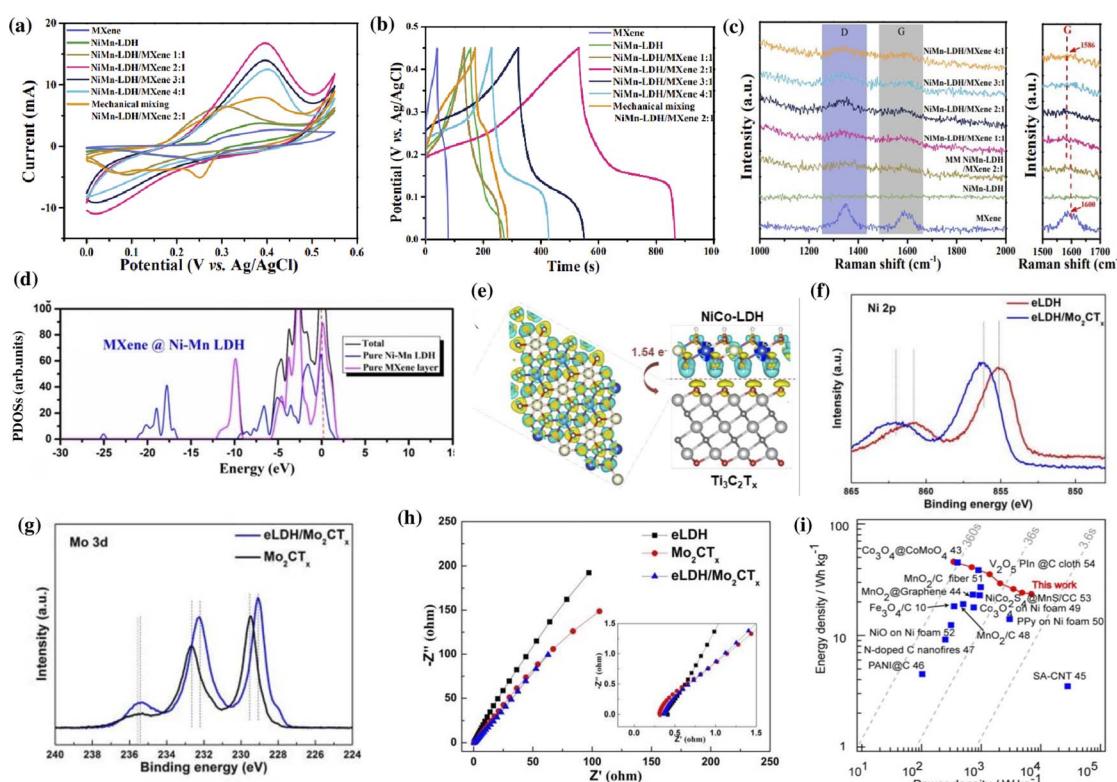

Fig. 4 (a) Cyclic voltammetry (CV) curves, (b) galvanostatic charge–discharge (GCD) curves, and (c) Raman spectra of MXene, NiMn-LDH, and NiMn-LDH/MXene hybrid nanocomposites. The CV and GCD curves were recorded at a scan rate of 5 mV s^{-1} and a current density of 2 A g^{-1}, respectively. Reproduced with permission from ref. 34 copyright 2020, American Chemical Society. (d) The calculated PDOS of MXene@Ni–Mn LDH. Reproduced with permission from ref. 37 copyright 2020, Elsevier. (e) Structure of charge difference distribution at the interface between NiCo-LDH and NiCo-LDH/$Ti_3C_2T_x$ composites. Reproduced with permission from ref. 122 copyright 2022, American Chemical Society. Comparison of the (f) Ni 2p and (g) Mo 3d fine XPS spectra of eLDH/Mo_2CT_x with pure eLDH or Mo_2CT_x nanosheets. (h) Nyquist plots for eLDH/Mo_2CT_x, pure eLDH, and Mo_2CT_x MXene. Reproduced with permission from ref. 149 copyright 2022, American Chemical Society. (i) Ragone plot of average power density vs. energy density for the fabricated Ti_3C_2/Ni–Co–Al-LDH//AC all-solid-state flexible asymmetric supercapacitor device. Reproduced with permission from ref. 151 copyright 2017, American Chemical Society.

14478 | J. Mater. Chem. A, 2023, **11**, 14469–14488

This journal is © The Royal Society of Chemistry 2023
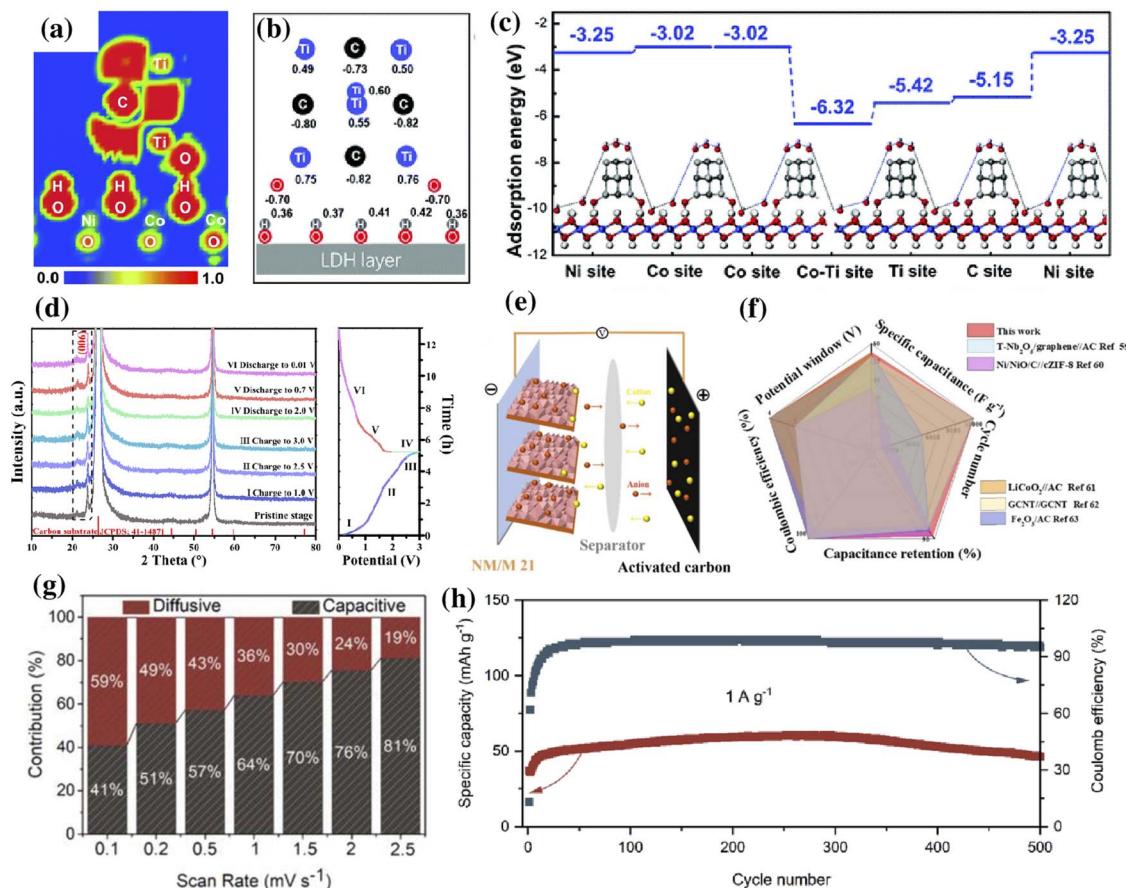
Fig. 5 (a) ELF mappings and (b) calculated charge of surface atoms of MQDs in Ni–Co LDH@MQDs. (c) Calculated adsorption energies using hydroxide (OH^-) as an example for Ni–Co LDH@MQDs (ref. 153). (d) *Ex situ* XRD patterns of NM/M 21 collected at various states, (e) schematic diagram of a NM/M 2 : 1//AC capacitor, and (f) comparison of its electrochemical performance with that of previously reported ASC devices. Reproduced with permission from ref. 154 copyright 2020, American Chemical Society. (g) Capacitive and diffusive contribution ratio of NiFe-LDH/MXene at respective scan rates. (h) Cycle stability of the NiFe-LDH/MXene//AC LIC at 1 A g^{-1}. Reproduced with permission from ref. 152 copyright 2021, American Chemical Society.

one hand, the 3D interconnected network of uniformly distributed LDH on the conductive MXene substrate offers substantial electrochemically active sites for electrolyte penetration, resulting in enhanced electrochemical reactions (Fig. 3b).[138,143] The 3D hierarchical porous structure also provides ion diffusion channels, promoting the rapid diffusion of ions and enhancing the specific capacity.[137] Furthermore, the 3D structures mitigate the volume change of the electrode during the charge–discharge process, and the strong bonding between the two 2D materials accelerates the electron transfer rate resulting in higher specific capacitance and cycling stability.[37] On the other hand, the face-to-face assembly of the MXene/LDH heterostructure delivers high volumetric capacity, high electrical conductivity, and a large surface area.[33]

The vertical array architecture effectively prevents the aggregation of catalysts, providing a large surface area and active sites for electrocatalysis (Fig. 3i).[118,144] Thus, the "house of cards" structure is an ideal morphology for the easy diffusion and transportation of gases on the surface of the electrocatalyst.[118] In a face-to-face MXene/LDH hybrid assembly, gas bubbles might be trapped between the layers, and thus the

morphology might not be as effective as the vertical array architecture for gas evolution reactions.

A core–shell morphology of the MXene/LDH hybrid with an increased specific surface area and active sites is beneficial for photocatalytic applications.[44] When the MXene is coupled with a semiconductor such as LDHs, an interfacial Schottky junction is generated, boosting the migration and separation of charge carriers. Thus, constructing a 2D/2D MXene/LDH heterostructure with a core–shell morphology is best suited for photocatalysis. Although a specific synthetic route is not designated to produce a specific morphology of MXene/LDH heterostructures, the experimental conditions of the common synthetic routes could be carefully tuned to obtain them.

4. Applications of MXene/LDH hybrids

The strong interfacial interactions and electronic coupling between the MXene and LDH in MXene/LDH heterostructures impart unique characteristics such as improved electronic

This journal is © The Royal Society of Chemistry 2023

J. Mater. Chem. A, 2023, **11**, 14469–14488 | **14479**

conductivity, active sites, and mechanical, structural, and chemical stability beneficial for various applications.[26,44,121,138,140,146,147] An in-depth understanding of the effects of heterointerface engineering and interactions at the heterointerface is crucial for the elicitation of synergy. To this end, this section discusses how the synergistic interactions at the heterointerface contribute to the overall properties of the MXene/LDH composite. The enhancement in the electrochemical properties favorable for energy applications is highlighted in particular.

4.1 Supercapacitors

The synergistic effects of MXene/LDH composites significantly enhance the conductivity, electrolyte accessibility, charge transfer rate, ion diffusion rate, and kinetics of redox reactions.[34,117,146] Besides inhibiting the restacking of sheets, the interstratification of the MXene and LDH increases the interlayer spacing of the composite, which provides abundant active sites and accelerates the diffusion of electrolyte ions.[128,148] Moreover, the strong electronic coupling between the MXene and LDH improves structural stability enabling long-term cycling.[37] All of these advantages are highly desirable for improving the charge storage capacity of supercapacitors.

The synergistic interactions in NiMn-LDH/Ti$_3$C$_2$ hybrid composites promote an improved rate capability, capacitance retention, and specific capacitance of 1575 F g^{-1} at 0.5 A g^{-1} (Fig. 4a and b).[34] The improved performance was mainly attributed to the accelerated electron transfer and ion diffusions at the interface of NiMn-LDH and Ti$_3$C$_2$, as evidenced by the shift in the G peak of the Raman spectrum (Fig. 4c). The chemical bonding between the uniformly distributed NiMn-LDH nanosheets on the surface of Ti$_3$C$_2$ MXene improved the reversibility and stability of the material, effectively preventing the aggregation and oxidation of the MXene. The interactions at the interface of MXene/LDH were further corroborated by partial density of states (PDOS) analysis.[37,138,143] The enhancement in the PDOS of Ti$_3$C$_2$@NiMn-LDH compared to its pristine counterparts around the Fermi region, as shown in Fig. 4d, points to the synergistic interfacial interactions due to the presence of abundant electrical transport pathways to facilitate ion mobility.[37] The continuous electronic states around the Fermi level lead to the metallic nature of the Ti$_3$C$_2$@NiMn-LDH composite. At the interfaces of MXene/LDH, the electrons are transferred from the OH$^-$ of the LDH to the O atoms in the MXene, indicating the presence of strong bonds and transport channels perpendicular to the layers.[143]

Wang *et al.* performed density functional theory (DFT) calculations to measure the interfacial energy and electron transport in a NiCo-LDH/Ti$_3$C$_2$T$_x$ composite.[122] An interlayer spacing of 1.77 Å and an interfacial adhesion energy of -5.1 eV indicated a strong interaction between the NiCo-LDH and Ti$_3$C$_2$T$_x$. The mesoporous layered architecture of the hybrid provided numerous ion transfer channels, which boost the electron transfer of about 1.54 e per unit cell from the less conductive NiCo-LDH to the highly conductive Ti$_3$C$_2$T$_x$, as shown in Fig. 4e. The close interaction of the MXene and LDH

was further confirmed by the presence of an intensive density of states (DOS) at the conduction band, which reduced the energy barrier for electron transfer and improved the conductivity of the MXene/LDH composite.[37,122,138] With stable interfacial interactions, the NiCo-LDH/Ti$_3$C$_2$T$_x$ heterostructure exhibited an outstanding rate capacity (85.2% from 1 to 10 A g^{-1}) and capacitance retention (80.4% after 5000 cycles).[122] Moreover, the supercapacitive performance of MXene/LDH also depends on the type of electrolyte used. Ti$_3$C$_2$T$_x$/NiCo-LDH exhibited the best performance in the alkaline electrolyte as the available hydroxyl ions promoted the activity of NiCo-LDH and reacted with the –F terminations on Ti$_3$C$_2$T$_x$ MXene, improving the overall performance of the composite.[127] Wu *et al.* reported that the hydration of 2D electrodes and exchange or adsorption of interlayer anions and cations in Ti$_3$C$_2$/NiCo-LDHs enabled the composite to deliver a specific capacitance of 1207 F g^{-1}, higher than the MXene (346 F g^{-1}) and NiCo-LDH (896 F g^{-1}) at 0.5 A g^{-1}.[128]

Trimetallic LDHs potentially exhibit better electrochemical properties than bimetallic LDHs as the incorporation of a third metal can alter the electronic structure of the host bimetallic LDH.[120,149] Liu *et al.* reported the increased availability of active sites for faradaic reactions in a composite comprising alkaline etched NiMnZn LDH and Mo$_2$CT$_x$ MXene.[149,150] The alkaline etching of NiMnZn LDH increased the oxygen vacancies and regulated the valence states of Ni/Mn. When the alkaline etched NiMnZn LDH (eLDH) was combined with Mo$_2$CT$_x$ MXene, the synergy between the two components further modified the electronic structure resulting in enhanced storage properties. X-ray photoelectron spectroscopy (XPS) analysis showed a shift in the binding energies of Ni, Mn, Zn, and O towards higher energy in contrast to the lower energy shift of Mo (Fig. 4f and g). This shift in peaks indicated a strong coupling between eLDH and Mo$_2$CT$_x$, suggesting the transfer of electrons from eLDH to Mo$_2$CT$_x$. The Mo$_2$CT$_x$ can reduce the internal resistance of eLDH (Fig. 4h) and enhance the overall stability of the composite. The Ti$_3$C$_2$/NiCoAl-LDH with molecular-level nanosheets exhibited the highest efficiency for charge transfer and the shortest diffusion pathway.[151] The densely packed alternative layers in the heterostructure enabled them to exhibit an energy density of 45.8 W h kg^{-1} at a power density of 346 W kg^{-1} when used as a positive electrode in an all-solid-state flexible asymmetric supercapacitor (Fig. 4i).

The synergistic interfacial interactions between the MXene and LDH could be optimized by modulating the MXene : LDH ratio, resulting in enhanced supercapacitive performance. It has been widely reported that the low amounts of MXene in the MXene/LDH hybrid lead to enhanced activity by preserving the active sites of the LDH from being masked by the lamellar structure of the MXene.[122] In addition, controlling the size and distribution of the *in situ* grown LDH on the MXene has been necessary to accelerate the ion diffusion at high current density.[34] Furthermore, the arrangement of the 2D sheets plays a crucial role in energy storage applications. For example, the face-to-face assembly of MXene/LDH hybrids, usually created through electrostatic interstratification, accelerates the diffusion of electrolyte ions, shortens the electron transfer path, and

14480 | *J. Mater. Chem. A*, 2023, **11**, 14469–14488

This journal is © The Royal Society of Chemistry 2023
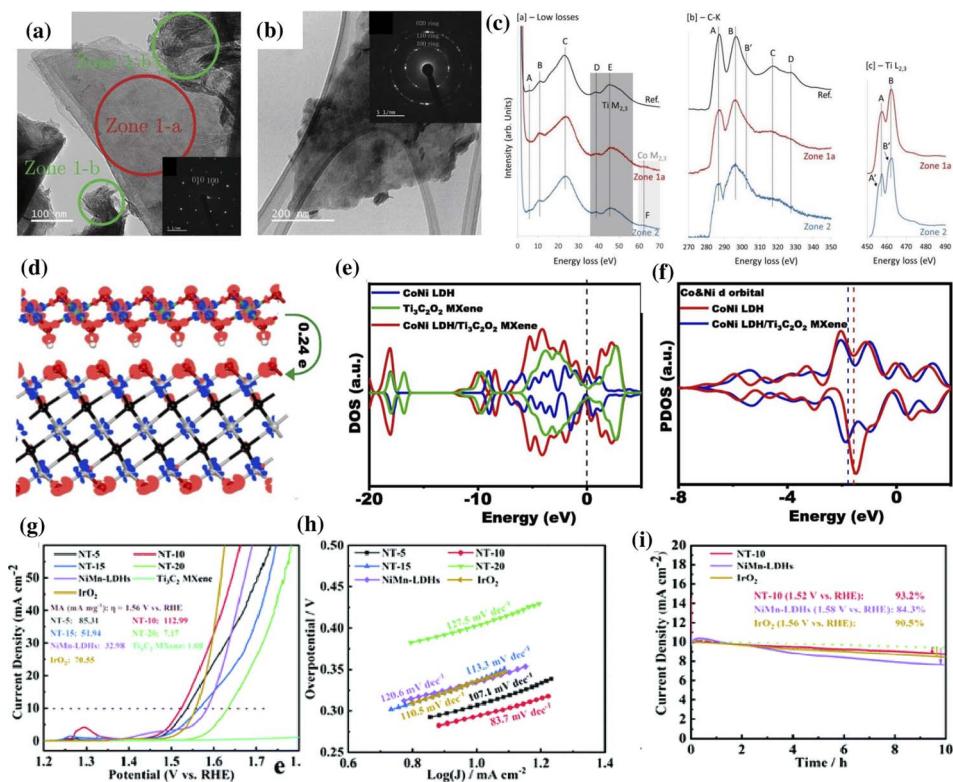
Fig. 6 TEM image depicting the (a) clean stack of $Ti_3C_2T_x$ sheets (Zone 1-a), fibrous Co-LDH (Zones 1-b), and (b) MXene covered with Co (Zone 2). The corresponding low loss spectra, C−K edge, and Ti $L_{2,3}$ edge recorded in Zones 1-a and 2 are shown in (c). Reproduced with permission from ref. 156 copyright 2019, Wiley. (d) Charge distribution in the CoNi LDH/$Ti_3C_2O_2$ composite, (e) DOS of CoNi LDH, $Ti_3C_2O_2$, and CoNi LDH/$Ti_3C_2O_2$ composites with the Fermi level at zero. (f) PDOS of the Co and Ni 3d orbitals of bare CoNi LDH and CoNi LDH/$Ti_3C_2O_2$ composites. Reproduced with permission from ref. 135 copyright 2020, Elsevier. (g) Linear sweep voltammetry, (h) Tafel slope, and (i) long-term stability curves of NiMn-LDHs/Ti_3C_2-MXene (ref. 140).

improves electrical conductivity.[33] The interconnected 3D morphology of the MXene/LDH hybrid can mitigate the volume change of the electrode during the charge–discharge process and accelerate the electron–electrolyte movement.[37] Thus, the prudent selection of LDH and MXene materials and an appropriate hybridization technique is critical to developing high-performance electrode materials for energy storage applications.

4.2 Metal-ion capacitors and batteries

As discussed earlier, by combining MXenes and LDHs, the self-stacking issue in the former and the poor conductivity of the latter could be effectively addressed. This combination results in a higher specific area and intercalation of metal ions, effectively improving the storage performance of metal-ion batteries and metal-ion capacitors.[146,152] Using theoretical models, Song et al. described the effect of interface coupling between MXene quantum dots (MQDs) and NiCo-LDH for enhanced storage activity of metal-ion batteries (∼140 mA h g^{-1} at 1 A g^{-1}).[153] The electron location function (ELF) mapping obtained by DFT was used to determine the bond strength and electron distribution. The ELF mapping in NiCo-LDH@MQD (Fig. 5a) indicates the presence of abundant electrons near "–Ti–O–H–O–", which were beneficial for strong interfacial coupling. A charge redistribution

was observed upon the addition of MQD to NiCo-LDH. Due to the interaction between the MQD and NiCo-LDH, the Ni and Co atoms gained 0.01–0.06 e, and O atoms lost 0.01–0.1 e (Fig. 5b). Furthermore, the adsorption energy for the hydroxide of the hybrid was higher than that of NiCo-LDH (Fig. 5c).

The metal-ion capacitor is a hybrid storage device consisting of a supercapacitor-type cathode and a battery-type anode.[152] Zhang et al. reported that the presence of an oxygen bridge at the interface of Ti_3C_2 MXene and NiMn-LDH promotes the diffusion of Li ions while maintaining excellent reversibility of the NiMn-LDH/Ti_3C_2 electrode during charging/discharging.[154] The structural evolution and the reaction mechanism of NiMn-LDH/Ti_3C_2 with a mass ratio of 2 : 1 (NM/M 21) were elucidated using ex situ XRD. The charging and discharging process was divided into six stages, and XRD was performed in different stages. As shown in Fig. 5d, there was no apparent change in the characteristic peak (006) located at 23.76° for the first three charging stages (I, II, and III); however, a mild shift towards the right was observed in the subsequent charging process (IV), indicating a phase change. During the discharging process (stages V and VI), the (006) shifted back towards the left to 23.61°. This shift in the peak during charging and discharging indicates change in the d spacing due to the Li$^+$ insertion. The absence of change in crystallinity after 1000 cycles indicated the

This journal is © The Royal Society of Chemistry 2023

J. Mater. Chem. A, 2023, 11, 14469–14488 | 14481

highly reversible nature of NM/M 21. Utilizing the fast electron transport characteristics at the interface, the Li-ion capacitor (LIC) (Fig. 5e and f) composed of a NM/M 21 anode and activated carbon (AC) cathode provided a high energy density of 122.7 W h kg^{-1} at a power density of 199 W kg^{-1} in a wide working voltage range (0.01–4.0 V).

In their following studies, the group extensively investigated the lithium storage properties of NiFe-LDH/Ti$_3$C$_2$ and Co-LDH/Ti$_3$C$_2$ hybrids.[146,152] The NiFe-LDH/Ti$_3$C$_2$ hybrid exhibited good storage performance when employed as an anode for Li-ion batteries (LIBs) and LICs.[152] In a lithium-ion half-cell, the NiFe-LDH/Ti$_3$C$_2$ electrode exhibited both diffusion-controlled battery and capacitive behavior, attributed to the interfacial interaction of NiFe-LDH and MXene. The increase in the capacitive contribution with the increase in the scan rate (Fig. 5g) indicated the excellent charge–discharge capability of the NiFe-LDH/Ti$_3$C$_2$ hybrid. A reversible capacity of 46.7 mA h g^{-1} with a coulombic efficiency of 96% at 1 A g^{-1} was recorded for the NiFe-LDH/Ti$_3$C$_2$//AC LIC after 500 cycles (Fig. 5h). On the other hand, the Co-LDH/Ti$_3$C$_2$ hybrid synthesized through a self-sacrificial template strategy exhibited a reversible capacity of 854.9 mA h g^{-1} at 0.1 A g^{-1} when tested as a LIB anode.[146] Similarly, the uniform nanoarrays of NiFe-

LDH on Ti$_3$C$_2$ exhibited high electrical conductivity and excellent electrochemical performance with a reversible specific capacity of 894.8 mA h g^{-1} at 200 mA g^{-1} when employed as a LIB anode.[155]

4.3 Electrocatalysis

MXene/LDH hybrid electrocatalysts tend to outperform their pristine counterparts and commercial catalysts with a lower overpotential and Tafel slope for water oxidation.[39,140] The facile charge transfer between the LDH and MXene endows the hybrid catalysts with significant adsorption/desorption balance, which accelerates the reaction kinetics during water splitting.[39,41,156] Additionally, the high metallic conductivity and the hydrophilic surface of the MXene aid in improving the catalytic activity of the MXene/LDH hybrid.[135,157]

The Ti$_3$C$_2$ MXene undergoes irreversible surface oxidation at $\approx$0.45 V (vs. Ag/AgCl), forming TiO$_2$ clusters, consequently undermining its stability.[156] This change in the surface electronic properties at required potentials for the OER is a significant drawback of the MXene. To resist the oxidation of the MXene during the OER, the uniform nucleation and growth of Co-LDH on the surface of conductive Ti$_3$C$_2$T$_x$ was reported as a viable strategy. The synergistic electronic interactions between the LDH and

Table 2 Summary of the performance of MXene/LDH hybrids in various applications[a]

Nanocomposite	Synthesis method	Application	Performance	Ref.
NiFe-LDH/Ti$_3$C$_2$	Hydrothermal	Supercapacitor	C_s = 720.2 F g^{-1} at 1 A g^{-1}	30
Ti$_3$C$_2$Cl$_2$@NiAl-LDH	Electrostatic interstratification	Supercapacitor	C_s = 2010.8 F g^{-1} at 1 A g^{-1}	162
V$_2$CT$_x$/NiV-LDH	Hydrothermal	Supercapacitor	C_s = 1658.19 F g^{-1} at 1 A g^{-1}	117
FeNi-LDH/Ti$_3$C$_2$T$_x$	In situ assembly	Supercapacitor	C_s = 922.6 F g^{-1} at 1 A g^{-1}	138
Ti$_3$C$_2$T$_x$/NiCo-LDH	Magneto-electrodeposition	Supercapacitor	C_a = 3.12 C cm^{-2} at 1 mA cm^{-2}	137
Ti$_3$C$_2$/CoAl-LDH	Electrostatic	Supercapacitor	C_v = 2472 C cm^{-3} at 1 A g^{-1}	33
Ti$_3$C$_2$@NiMn-LDH	Coprecipitation	Supercapacitor	C_s = 179 mA h g^{-1} at 1 A g^{-1}	37
Ti$_3$C$_2$/ZnMnNi-LDH	Electrostatic self-assembly	Supercapacitor	C_s = 2065 F g^{-1} at 5 mV s^{-1}	120
Ti$_3$C$_2$/NiCoAl-LDH	Electrostatic	Supercapacitor	C_s = 748.2 F g^{-1} at 1 A g^{-1}	151
Ti$_3$C$_2$/NiCoFe-LDH	Hydrothermal	Supercapacitor	C_s = 1190 F g^{-1} at 1 A g^{-1}	35
NiFe-LDH/Ti$_3$C$_2$	Hydrothermal	LIC	ED = 168 W h kg^{-1} at PD = 47 W kg^{-1}	152
NiMn-LDH/Ti$_3$C$_2$	In situ crystallization	LIC	ED = 122.7 W h kg^{-1} at PD = 199 W kg^{-1}	154
Co-LDH/Ti$_3$C$_2$	In situ growth	LIB	C_r = 854.9 mA h g^{-1} at 0.1 A g^{-1}	146
NiCo-LDH@Ti$_3$C$_2$	Hydrothermal	Battery	C_s = 140 mA h g^{-1} at 1 A g^{-1}	153
NiFe-LDH/Ti$_3$C$_2$	Refluxing	LIB	C_d = 894.8 mA h g^{-1} at 200 mA g^{-1}	155
Co-LDH@Ti$_3$C$_2$T$_x$	Polyol process	OER	η = 330 mV at 10 mA cm^{-2}	156
FeNi-LDH/V$_2$C	Hydrothermal	OER	η = 250 mV at 10 mA cm^{-2}	39
CoNi-LDH/Ti$_3$C$_2$T$_x$	Electrodeposition	OER	257.4 mV at 100 mA cm^{-2}	135
CoFe–P/Ti$_3$C$_2$T$_x$	Hydrothermal	OER	η = 270 mV at 10 mA cm^{-2}	158
CoFe-LDH/Ti$_3$C$_2$T$_x$	In situ growth	OER	η = 319 mV at 10 mA cm^{-2}	40
NiMn-LDH/Ti$_3$C$_2$T$_x$	Hydrothermal	OER	η = 294 mV at 10 mA cm^{-2}	140
Ti$_3$C$_2$/NiCo-LDH	Hydrothermal	Glucose sensor	Limit of detection = 0.53 μM	26
Ti$_3$C$_2$/NiCo-LDH	Hydrothermal	EMW absorption	EAB = 4.48 GHz	50
Ti$_3$C$_2$T$_x$@MOF-LDH	Hydrothermal	Inhibits fire and toxic smoke hazards of FPUF	16.1% reduction in smoke	160
NiFe-LDH/Ti$_3$C$_2$T$_x$	Hydrothermal	Photodegradation of norfloxacin	98% degradation in 4 h	115
Co–Co LDH/Ti$_3$C$_2$T$_x$	In situ synthesis	Photocatalytic CO$_2$ reduction	CO$_2$ to CO evolution rate = 1.25 × 10^4 μmol h^{-1} g^{-1}	45
NiAl-LDH/Ti$_3$C$_2$T$_x$	Hydrothermal	Photocatalytic CO$_2$ reduction	CO$_2$ to CO evolution rate = 2128.46 μmol h^{-1} g^{-1}	44

[a] C_s = specific capacitance, C_a = areal capacitance, C_v = volumetric capacity, ED = energy density, PD = power density, C_r = reversible capacity, C_d = discharge capacity, η = overpotential, EMW = electromagnetic wave absorption, and EAB = effective absorption bandwidth.

14482 | J. Mater. Chem. A, 2023, **11**, 14469–14488

This journal is © The Royal Society of Chemistry 2023

MXene promote the catalytic activity of Co-LDH/Ti_3C_2 towards the OER, displaying an overpotential of 330 mV at 10 mA cm^{-2}. The TEM images of the MXene sheet (Zone-1a), fibrous Co-LDH (Zone-1b), and Co-LDH on MXene (Zone-2) are shown in Fig. 6a and b. Their corresponding electron energy loss spectroscopy (EELS) spectra are shown in Fig. 6c. Notably, the F region in the low loss spectra corresponds to the Co $M_{2,3}$ edge, indicating the presence of Co on the MXene. The broadening of peaks at the C–K edge and the slight splitting of peaks at the Ti $L_{2,3}$ edge recorded in Zone-2 imply the electronic modification of $Ti_3C_2T_x$. However, the peaks at the Ti $L_{2,3}$ edge of Zone 1 are similar to those of the reference ($Ti_3C_2T_x$), indicating the unchanged inner structure of the MXene.

DFT calculation is a versatile tool for understanding the synergy of MXene and CoNi LDH.[135,140] In a CoNi-LDH/$Ti_3C_2O_2$ hybrid system, the transfer of electrons from Co and Ni to other atoms is evident from the charge depletion observed around the metal atoms Co and Ni (Fig. 6d).[135] The changes in the electronic structure were investigated using the density of states (DOS) and projected DOS analysis, as shown in Fig. 6e and f, respectively. The increased DOS near the Fermi level indicates the synergistic electronic interactions beneficial for charge transfer. A negative shift in the d-band center of the Co and Ni atoms in the MXene/hybrid system compared to CoNi LDH indicates a reduction in the binding energy of the intermediates (*OH, *O, and *OOH) on the surface of CoNi LDH during the OER. With such optimized binding energy, the CoNi LDH/$Ti_3C_2O_2$ hybrid exhibited a small Tafel slope of 68 mV dec^{-1} and a turnover frequency of 0.37 s^{-1} at an overpotential of 300 mV. Liu et al. evaluated the lattice shrinkage of the LDH in the MXene/LDH hybrid by analyzing the layer distance between Ni–O (8.608 Å) and Mn–O (8.645 Å) in NiMn-LDHs/Ti_3C_2.[140] The strain effect caused by this lattice shrinkage was reported to be beneficial for optimizing the electronic structure and surface adsorption energy during the OER. The NiMn-LDHs/Ti_3C_2 hybrid showed an overpotential of 294 mV at a current density of 10 mA cm^{-2}, a Tafel slope of 83.7 mV dec^{-1}, and stability higher than the commercial IrO_2 catalyst (Fig. 6g–i).

The electrocatalytic activity of MXene/LDH composites can be enhanced by varying the intercalated anions and/or introducing heteroatoms.[39,158] Chen et al. reported that hypophosphite groups ($H_2PO_2^-$) intercalated as anions in LDHs enhanced the OER activity of V_2C/FeNi-LDH.[39] Compared to CO_3^{2-} intercalated FeNi-LDH/V_2C, the $H_2PO_2^-$ intercalated FeNi-LDH/V_2C had optimized binding energy and facilitated the charge transfer from the LDH to V_2C, achieving higher catalytic activity. The $H_2PO_2^-$ intercalated FeNi-LDH/V_2C exhibited outstanding stability with no change in current density for about 30 000 s. The electrocatalytic performance of CoFe-LDH/$Ti_3C_2T_x$ could be further improved by introducing heteroatoms such as P or S into CoFe-LDH.[158] The phosphorization of CoFe-LDH results in the transfer of electrons from Co and Fe to P, which promotes the valence state of Co and Fe for easy adsorption of oxygen in the intermediate state.

4.4 Other notable applications

The synergistic interactions of MXene/LDH hybrids are also reported to be conducive to their performances in sensors, photocatalytic degradation, anticorrosion, antiwear, wastewater treatment, toxic smoke inhibition, etc.[115,119,159,160] MXene/LDH composites are highly suitable for photocatalytic applications with an increased specific surface area and abundant active sites.[45] In the case of ZnCr-LDH/$Ti_3C_2T_x$ heterostructures, the Fermi energy of ZnCr-LDH is higher than that of $Ti_3C_2T_x$; hence the electrons from ZnCr-LDH are driven to $Ti_3C_2T_x$ to equilibrate the Fermi energy between them.[47] During photocatalysis, the energy band of ZnCr-LDH bends upwards, producing a Schottky barrier. Under light irradiation, the photogenerated electrons migrate along the Schottky junction to the MXene, achieving effective electron separation. The formed Schottky barriers prevent the backflow of electrons to the LDH and reduce the recombination rate of the photo-excited carriers.[44] The electrons accumulated in the Fermi energy of MXene react readily with the adsorbed CO_2 molecules and convert them to CO and CH_4 gas. Thus, the increased photogenerated electron separation, migration of charge carriers along the interface of MXene/LDH, and suppressed back-diffusion of electrons contribute to the enhanced photocatalytic CO_2 reduction performance compared to their pristine counterparts. The same phenomenon was observed in the photocatalytic degradation of norfloxacin, acetaminophen, and ibuprofen, the commonly detected pharmaceuticals in water.[115,161]

MXene/LDH hybrids are also used as chloride ion storage electrodes in capacitive deionization and as adsorbents for the removal of carcinogenic Ni(III) in water treatment.[121,159] The large interface contact area of the MXene/LDH structure provides abundant active sites for the adsorption of heavy metals, and their micro–mesoporous structure establishes pathways to accelerate ion diffusion and enhance the desalination rate.

MXene/LDH hybrids exhibit synergistic effects of magnetic loss, dielectric loss, and excellent attenuation capability, making them suitable for use as electromagnetic wave absorbers.[50] The heterojunction formed on the surface of the hybrid promotes effective dissipation of electromagnetic waves. Furthermore, the excellent dispersibility and compatibility of $Ti_3C_2T_x$ MXene@MgAl-LDH with epoxy resin enhance the anticorrosion and antiwear abilities of the epoxy coating.[119] $Ti_3C_2T_x$ MXene aids in improving the anticorrosion and antiwear abilities of the epoxy coating, and the restacking of MXene could be prevented by the LDH, which also acts as a nanocontainer for corrosion inhibition.

MXene/LDH hybrids also reduce the toxic smoke produced by polyurethane foam (FPUF) combustion.[160] An LDH derived from the ZIF-67 metal–organic framework (MOF-LDH) was hybridized with $Ti_3C_2T_x$ and then added to FPUF. 6 wt% $Ti_3C_2T_x$@MOF-LDH (MOF-HDH) added to the FPUF reduced the total smoke production by 16.1%. Besides reducing the smoke and fire hazards of FPUF, the FPUF/$Ti_3C_2T_x$@MOF-LDH hybrid achieved excellent mechanical properties with increased compressive and tensile strength. MXene/LDH hybrids have been reported to be applicable for detecting biomarkers, fungicides, glucose, etc.[48,116,147] The synergetic effects of the MXene and LDH in the hybrid, interfacial interaction through chemical bonds, adequate number of active sites, short diffusion pathways increasing the charge-transfer rates, and the large ion-accessible surface area enable the MXene/LDH hybrid to be used in sensor applications.

This journal is © The Royal Society of Chemistry 2023

J. Mater. Chem. A, 2023, 11, 14469–14488 | 14483

5. Summary

Individually, MXenes and LDHs are fascinating 2D structured materials. Since their discovery in 2011, MXenes have attracted huge attention from energy research communities due to their favorable electronic and physical properties, such as high electrical conductivity, large surface area, and tuneable structure. Likewise, the excellent redox capability, incomparable theoretical capacitance, low cost, and facile scalability of LDHs have greatly encouraged researchers to exploit them in various applications. However, MXenes and LDHs have their respective shortcomings, such as relatively low capacitance and poor electrical conductivity. In this regard, the hybridization of MXenes and LDHs successfully counterbalances the significant drawbacks of each component and ameliorates their restacking and inherent stability problems to some extent. This review pays particular attention to the formation mechanism of 2D/2D heterostructures of MXenes and LDHs, the alteration of the structure and properties, the interfacial interaction at the heterointerface, and the application progress of MXene/LDH hybrids.

The formation of the MXene/LDH hybrid is based on two main strategies: electrostatic assembly driven by oppositely charged 2D monolayers and the direct growth of LDHs on the surface of MXenes. Since the electrostatic assembly is carried out by physically mixing pre-synthesized MXenes and LDHs, it can be considered a more general strategy to combine various compositions of MXenes and LDHs physically. On the other hand, more intimate and chemically bound heterointerfaces are established *via* the direct growth of LDHs on pre-synthesized MXenes. Thus, the second strategy is perceived to intensify the synergistic interaction between the electronic properties of MXenes and LDHs. Regardless of the synthetic strategy, reduced restacking and an enhanced active surface area have been observed in the MXene/LDH hybrids. The outstanding synergistic effects originating from their heterointerfaces inspired many researchers to utilize MXene/LDH hybrids for various applications (Table 2).

We presented several studies with theoretical calculations to investigate the contributions of the interfacial interactions at the heterointerfaces to the electrochemical performance. It was revealed that the electronic coupling between the MXene and LDH in MXene/LDH heterostructures induces unique characteristics such as improved electronic conductivity, active sites, and mechanical, structural, and chemical stability. Charge redistribution can occur upon the formation of a heterointerface, changing the electron density of the constituent elements, resulting in strong interfacial coupling and enhanced mechanical and chemical stability of the heterostructures. In addition, such charge redistribution can affect the electronic properties of the surface to promote electrochemical activity. Overall, the resulting MXene/LDH hybrids have shown impressive results.

6. Challenges and prospects

The following challenges have been identified as urgent for the development of MXene/LDH hybrids.

6.1 Lack of scalable synthetic methods

While a variety of LDHs can be easily synthesized under mild conditions, the synthesis of MXenes requires severe reaction conditions, including high temperature/pressure and toxic etching methods, which pose difficulties in regulating the important qualities of MXenes, such as size, defects, composition, and the number of layers. The major drawback of MXenes is their surface oxidation, which limits their large-scale applications. Although it has been reported that *in situ* anchoring of highly dispersed LDH nanosheets on MXene sheets *via* chemical bonds reduces the surface oxidation of MXenes, fine-tuning the composite is necessary to obtain optimal performance. By changing the synthesis conditions, interfacial chemistry, and LDH content, surface oxidation may be controlled, and the MXene/LDH composite's characteristics can be optimized. Therefore, it is worth putting effort into finding a safe, efficient, and environmentally friendly preparation method to obtain quality-controlled MXenes on a large scale.

The present methods may be simple and applicable to various combinations of MXenes and LDHs; however, a limited number of synthetic routes are available for yielding quality MXene/LDH hybrids. Note that the product quality varies significantly in terms of layer-by-layer homogeneity, thickness, and elemental compositions. With this, developing innovative methods is crucial to control such factors so that the synergistic effects of the nanocomposites can be maximized and fine-tuned for targeted applications.

6.2 Lack of *in situ*/*operando* techniques

Most of the studies on MXene/LDH hybrids assume that the formation of 2D/2D heterostructures enhances the rate of ion diffusion, electron transfer, and mechanical/chemical stability based on their structural analysis and performance. Although such experimental results may suggest that the synergistic effects originated from the hybridization, the detailed picture of how each component synergistically affects each other is still unknown. In this regard, *in situ*/*operando* techniques with various spectroscopic tools (*i.e.*, infrared (IR) spectroscopy, Raman spectroscopy, XPS, and X-ray absorption near edge spectroscopy/extended X-ray absorption fine structure spectroscopy (XANES/EXFAS)) can provide clearer evidence of the interactions at the heterointerfaces.

Notably, the oxidation states of the composing elements can change dynamically during electrochemical operation, leading to the change in the state of chemical bonds between the atoms in a monolayer and between the monolayers. Hence, the synergistic effects observed in MXene/LDH hybrids should be elucidated *via in situ*/*operando* analyses to provide critical insights to optimize the structure and composition of the nanocomposites.

6.3 Not sufficient synthetic efforts to discover new structural designs

Expanding MXene/LDH hybrids to ternary and/or quaternary nanocomposites is an important research direction to further improve their electronic and mechanical properties. Compared

14484 | *J. Mater. Chem. A*, 2023, **11**, 14469–14488

This journal is © The Royal Society of Chemistry 2023

to binary composites, only a handful of reports have shown to interstratify foreign materials in MXene/LDH nanocomposites, insinuating that forming complex heterointerfaces by the introduction of additional material complicates the synthetic procedure and makes it more challenging to probe their properties. Nevertheless, the successful hybridization of MXenes, LDHs, and other hetero-species might result in unique electronic/mechanical properties, thus making it a highly attractive research direction.

Moreover, the number of transition metal (M) layers and the carbon and/or nitrogen (X) layers influence the electronic and chemical properties of MXenes. These structural variations can impact the interfacial coupling, charge redistribution, and stability of MXene–LDH heterojunctions, ultimately affecting their overall performance and functionality in various applications. Detailed studies are necessary to investigate the specific effects of each MXene structure (M_2X, M_3X_2, and M_4X_3) on MXene/LDH heterojunctions.

While addressing the challenges mentioned above, adopting a systematic approach for optimizing the MXene/LDH hybrid is crucial, considering both structural and compositional aspects. Undoubtedly, the two major application fields for MXene/LDH hybrids are electrochemical energy storage and electrocatalysis. Although these fields require different electronic and chemical properties, strategic approaches to choose the most efficient combination of MXenes and LDHs for specific applications have rarely been attempted. For electrochemical energy storage, the electrode material must accommodate significant volume expansion and contraction during charging and discharging, providing sufficient channels for facile ion diffusion. The heterostructures formed through electrostatic interactions may be more suitable under such operating conditions. Moreover the use of MXene/LDH hybrids as an anode and electrocatalyst has been limited to LICs/LIBs and the OER, respectively. Therefore, developing MXene/LDH hybrids with tailored compositions for other battery and electrocatalytic applications would be highly beneficial. Additionally, although MXene/LDH hybrids have displayed impressive electrochemical storage properties, their exact storage mechanism remains unclear. Further investigation into the relationship between the behavior of the hybrid material and electrochemical energy storage is essential.

7. Concluding remarks

Tremendous effort has been invested in the hybridization of MXenes and LDHs, and the resulting MXene/LDH heterostructures have shown impressive results in various energy applications. This review critically assesses the recent progress in developing MXene/LDH nanocomposites with a close look at their formation mechanisms and synergistic interactions. Thanks to intensive research on this topic, it is clear that the synergistic effects arise from the heterointerfaces created between the monolayers of MXenes and LDHs. However, continuous effort is still needed to fully unveil the potential of these unique 2D/2D heterostructures, and the remaining challenges must be appropriately tackled to reach the commercialization stage in the future. We hope that this review can point to fruitful research directions in MXene/LDH heterostructures, leading to innovative breakthroughs in material synthesis, design, and performance.

Conflicts of interest

The authors declare that they have no conflict of interest.

Acknowledgements

References

1 M. Xu, T. Liang, M. Shi and H. Chen, *Chem. Rev.*, 2013, **113**, 3766–3798.

2 S. Z. Butler, S. M. Hollen, L. Cao, Y. Cui, J. A. Gupta, H. R. Gutiérrez, T. F. Heinz, S. S. Hong, J. Huang and A. F. Ismach, *ACS Nano*, 2013, 7, 2898–2926.

3 Z. Sun and H. Chang, *ACS Nano*, 2014, **8**, 4133–4156.

4 G. R. Bhimanapati, Z. Lin, V. Meunier, Y. Jung, J. Cha, S. Das, D. Xiao, Y. Son, M. S. Strano and V. R. Cooper, *ACS Nano*, 2015, **9**, 11509–11539.

5 A. C. Ferrari, F. Bonaccorso, V. Fal'Ko, K. S. Novoselov, S. Roche, P. Bøggild, S. Borini, F. H. Koppens, V. Palermo and N. Pugno, *Nanoscale*, 2015, 7, 4598–4810.

6 M. Yoshizawa and M. Yamashina, *Chem. Lett.*, 2017, **46**, 163–171.

7 F. Wang, Z. Wang, L. Yin, R. Cheng, J. Wang, Y. Wen, T. A. Shifa, F. Wang, Y. Zhang and X. Zhan, *Chem. Soc. Rev.*, 2018, **47**, 6296–6341.

8 X. Li and L. Zhi, *Chem. Soc. Rev.*, 2018, **47**, 3189–3216.

9 K. Khan, A. K. Tareen, M. Aslam, Y. Zhang, R. Wang, Z. Ouyang, Z. Gou and H. Zhang, *Nanoscale*, 2019, **11**, 21622–21678.

10 E. S. Penev, N. Marzari and B. I. Yakobson, *ACS Nano*, 2021, **15**, 5959–5976.

11 F. R. Fan, R. Wang, H. Zhang and W. Wu, *Chem. Soc. Rev.*, 2021, **50**, 10983–11031.

12 Y. Huang, Q. Lu, D. Wu, Y. Jiang, Z. Liu, B. Chen, M. Zhu and O. G. Schmidt, *Carbon Energy*, 2022, **4**, 598–620.

13 G. Gao, S. Yang, S. Wang and L. Li, *Scr. Mater.*, 2022, **213**, 114605.

14 J. Tang, X. Peng, T. Lin, X. Huang, B. Luo and L. Wang, *eScience*, 2021, **1**, 203–211.

15 J. Liang, Y. Ge, Z. He, Q. Yun, G. Liu, S. Lu, L. Zhai, B. Huang and H. Zhang, *Nano Res.*, 2021, 1–21, DOI: **10.1007/s12274-021-4007-6**.

16 L. Lv, Z. Yang, K. Chen, C. Wang and Y. Xiong, *Adv. Energy Mater.*, 2019, **9**, 1970057.

17 Z. You, Y. Liao, X. Li, J. Fan and Q. Xiang, *Nanoscale*, 2021, **13**, 9463–9504.

18 X. Zhan, C. Si, J. Zhou and Z. Sun, *Nanoscale Horiz.*, 2020, **5**, 235–258.

19 S. Li, J. He, P. Nachtigall, L. Grajciar and F. Brivio, *Phys. Chem. Chem. Phys.*, 2019, **21**, 25802–25808.

20 N. Li, Y. Li and J. Fan, *Nanoscale*, 2021, **13**, 7234–7243.

21 Y. Li, L. Li, R. Huang, Y. Zhang and Y. Wen, *Nanoscale*, 2021, **13**, 2995–3001.

22 Y. Gafour, A. Hamidi, A. Benahmed, M. Zidour and T. Bensattalah, *Adv. Nano Res.*, 2020, **8**, 37–47.

23 H. Liang, J. Lin, H. Jia, S. Chen, J. Qi, J. Cao, T. Lin, W. Fei and J. Feng, *J. Mater. Chem. A*, 2018, **6**, 15040–15046.

24 J. Hu, Y. Ou, Y. Li, D. Gao, Y. Zhang and P. Xiao, *ACS Sustainable Chem. Eng.*, 2018, **6**, 11724–11733.

25 S. Liu, J. Zhu, M. Sun, Z. Ma, K. Hu, T. Nakajima, X. Liu, P. Schmuki and L. Wang, *J. Mater. Chem. A*, 2020, **8**, 2490–2497.

26 M. Li, L. Fang, H. Zhou, F. Wu, Y. Lu, H. Luo, Y. Zhang and B. Hu, *Appl. Surf. Sci.*, 2019, **495**, 143554.

27 J. Zheng, X. Pan, X. Huang, D. Xiong, Y. Shang, X. Li, N. Wang, W.-M. Lau and H. Y. Yang, *Chem. Eng. J.*, 2020, **396**, 125197.

28 K. Zhou, K. Gong, F. Gao and L. Yin, *Composites, Part A*, 2022, **157**, 106912.

29 B. Shen, H. Huang, Y. Jiang, Y. Xue and H. He, *Electrochim. Acta*, 2022, **407**, 139913.

30 H. Zhou, F. Wu, L. Fang, J. Hu, H. Luo, T. Guan, B. Hu and M. Zhou, *Int. J. Hydrogen Energy*, 2020, **45**, 13080–13089.

31 W. Almusattar, M. Tahir, M. Madi and B. Tahir, *J. Environ. Chem. Eng.*, 2022, **10**, 108010.

32 Z. Zhao, X. Wu, C. Luo and Y. Yang, *J. Power Sources*, 2022, **545**, 231910.

33 H. Niu, X. Yang, Q. Wang, X. Jing, K. Cheng, K. Zhu, K. Ye, G. Wang, D. Cao and J. Yan, *J. Energy Chem.*, 2020, **46**, 105–113.

34 D. Zhang, J. Cao, X. Zhang, N. Insin, R. Liu and J. Qin, *ACS Appl. Energy Mater.*, 2020, **3**, 5949–5964.

35 J. Chen, Y. Ren, H. Zhang, J. Qi, Y. Sui and F. Wei, *Appl. Surf. Sci.*, 2021, **562**, 150116.

36 C. Zhang, R. Guo, H. Wang, X. Xie and C. Du, *Appl. Surf. Sci.*, 2022, **598**, 153796.

37 W. Wang, D. Jiang, X. Chen, K. Xie, Y. Jiang and Y. Wang, *Appl. Surf. Sci.*, 2020, **515**, 145982.

38 M. Li, R. Sun, Y. Li, J. Jiang, W. Xu, H. Cong and S. Han, *Chem. Eng. J.*, 2022, **431**, 133941.

39 Y. Chen, H. Yao, F. Kong, H. Tian, G. Meng, S. Wang, X. Mao, X. Cui, X. Hou and J. Shi, *Appl. Catal., B*, 2021, **297**, 120474.

40 J. Sun, Y. Lin, Z. Sun, S. Zhu, R. Amal, F. Li and D.-W. Wang, *Mater. Today*, 2019, **14**, 100342.

41 M. Yu, J. Zheng and M. Guo, *J. Energy Chem.*, 2022, **70**, 472–479.

42 Y. Arakawa, K. Komatsu and H. Tsuji, *Phase Transitions*, 2022, **95**, 331–339.

43 X. Li, Z. Zhang, Q. Xiang, R. Chen, D. Wu, G. Li and L. Wang, *RSC Adv.*, 2021, **11**, 12392–12397.

44 S. Zhao, D. Pan, Q. Liang, M. Zhou, C. Yao, S. Xu and Z. Li, *J. Phys. Chem. C*, 2021, **125**, 10207–10218.

45 W. Chen, B. Han, Y. Xie, S. Liang, H. Deng and Z. Lin, *Chem. Eng. J.*, 2020, **391**, 123519.

46 A. Ali Khan and M. Tahir, *Ind. Eng. Chem. Res.*, 2021, **60**, 16201–16223.

47 B. Zhou, Y. Yang, Z. Liu, N. Wu, Y. Yan, Z. Wenhua, H. He, J. Du, Y. Zhang and Y. Zhou, *Nanoscale*, 2022, **14**, 7538–7546.

48 M. Zhang, L. Mei, L. Zhang, X. Wang, X. Liao, X. Qiao and C. Hong, *Bioelectrochemistry*, 2021, **142**, 107943.

49 B. Sriram, J. N. Baby, S.-F. Wang, R. Ranjitha M, M. Govindasamy and M. George, *ACS Sustainable Chem. Eng.*, 2020, **8**, 17772–17782.

50 X. Gao, Z. Jia, B. Wang, X. Wu, T. Sun, X. Liu, Q. Chi and G. Wu, *Chem. Eng. J.*, 2021, **419**, 130019.

51 S. Venkateshalu, M. Shariq, N. K. Chaudhari, K. Lee and A. N. Grace, *J. Mater. Chem. A*, 2022, **10**, 20174–20189.

52 N. Hemanth, T. Kim, B. Kim, A. H. Jadhav, K. Lee and N. K. Chaudhari, *Mater. Chem. Front.*, 2021, **5**, 3298–3321.

53 A. Liu, X. Liang, X. Ren, W. Guan, M. Gao, Y. Yang, Q. Yang, L. Gao, Y. Li and T. Ma, *Adv. Funct. Mater.*, 2020, **30**, 2003437.

54 K. Nasrin, V. Sudharshan, K. Subramani and M. Sathish, *Adv. Funct. Mater.*, 2022, **32**, 2110267.

55 X. Li, C. Wang, Y. Cao and G. Wang, *Chem.–Asian J.*, 2018, **13**, 2742–2757.

56 Z. Kang, M. A. Khan, Y. Gong, R. Javed, Y. Xu, D. Ye, H. Zhao and J. Zhang, *J. Mater. Chem. A*, 2021, **9**, 6089–6108.

57 J. Yu, F. Yu, M.-F. Yuen and C. Wang, *J. Mater. Chem. A*, 2021, **9**, 9389–9430.

58 C. Lamiel, I. Hussain, O. R. Ogunsakin and K. Zhang, *J. Mater. Chem. A*, 2022, **10**, 14247–14272.

59 S. De, S. Acharya, S. Sahoo and G. C. Nayak, *Mater. Chem. Front.*, 2021, **5**, 7134–7169.

60 A. Ali Khan, M. Tahir and N. Khan, *Energy Fuels*, 2022, **36**, 9821–9843.

61 H. Wang and J.-M. Lee, *J. Mater. Chem. A*, 2020, **8**, 10604–10624.

62 N. K. Chaudhari, H. Jin, B. Kim, D. San Baek, S. H. Joo and K. Lee, *J. Mater. Chem. A*, 2017, **5**, 24564–24579.

63 V. M. H. Ng, H. Huang, K. Zhou, P. S. Lee, W. Que, J. Z. Xu and L. B. Kong, *J. Mater. Chem. A*, 2017, **5**, 3039–3068.

64 J. A. Kumar, P. Prakash, T. Krithiga, D. J. Amarnath, J. Premkumar, N. Rajamohan, Y. Vasseghian, P. Saravanan and M. Rajasimman, *Chemosphere*, 2022, **286**, 131607.

65 J. Pang, R. G. Mendes, A. Bachmatiuk, L. Zhao, H. Q. Ta, T. Gemming, H. Liu, Z. Liu and M. H. Rummeli, *Chem. Soc. Rev.*, 2019, **48**, 72–133.

66 D. Nepal, W. J. Kennedy, R. Pachter and R. A. Vaia, *ACS Nano*, 2020, **15**, 21–28.

67 J. Thörnberg, J. Halim, J. Lu, R. Meshkian, J. Palisaitis, L. Hultman, P. O. Persson and J. Rosen, *Nanoscale*, 2019, **11**, 14720–14726.

68 M. Li, J. Lu, K. Luo, Y. Li, K. Chang, K. Chen, J. Zhou, J. Rosen, L. Hultman and P. Eklund, *J. Am. Chem. Soc.*, 2019, **141**, 4730–4737.

69 B. Anasori, J. Halim, J. Lu, C. A. Voigt, L. Hultman and M. W. Barsoum, *Scr. Mater.*, 2015, **101**, 5–7.

70 M. Khazaei, A. Ranjbar, M. Arai and S. Yunoki, *Phys. Rev. B*, 2016, **94**, 125152.

71 Y. Li, Y. Ding, B. Xiao and Y. Cheng, *Phys. Lett. A*, 2016, **380**, 3748–3755.

72 B. Anasori and Y. Gogotsi, *Nanoscale Horiz.*, 2020, **5**, 1557–1565, DOI: **10.151039/D156510NH100343C**.

73 S. Venkateshalu, G. M. Tomboc, B. Kim, J. Li and K. Lee, *ChemNanoMat*, 2022, **8**, e202200320.

74 R. Syamsai, J. R. Rodriguez, V. G. Pol, Q. Van Le, K. M. Batoo, S. F. Adil, S. Pandiaraj, M. Muthumareeswaran, E. H. Raslan and A. N. Grace, *Sci. Rep.*, 2021, **11**, 688.

75 M. Dahlqvist, A. Petruhins, J. Lu, L. Hultman and J. Rosen, *ACS Nano*, 2018, **12**, 7761–7770.

76 M. Khazaei, A. Ranjbar, K. Esfarjani, D. Bogdanovski, R. Dronskowski and S. Yunoki, *Phys. Chem. Chem. Phys.*, 2018, **20**, 8579–8592.

77 A. Thore and J. Rosén, *Phys. Chem. Chem. Phys.*, 2017, **19**, 21595–21603.

78 A. Petruhins, J. Lu, L. Hultman and J. Rosen, *Mater. Res. Lett.*, 2019, **7**, 446–452.

79 I. Persson, A. El Ghazaly, Q. Tao, J. Halim, S. Kota, V. Darakchieva, J. Palisaitis, M. W. Barsoum, J. Rosen and P. O. Persson, *Small*, 2018, **14**, 1703676.

80 C. E. Shuck, A. Sarycheva, M. Anayee, A. Levitt, Y. Zhu, S. Uzun, V. Balitskiy, V. Zahorodna, O. Gogotsi and Y. Gogotsi, *Adv. Eng. Mater.*, 2020, **22**, 1901241.

81 P. Urbankowski, B. Anasori, T. Makaryan, D. Er, S. Kota, P. L. Walsh, M. Zhao, V. B. Shenoy, M. W. Barsoum and Y. Gogotsi, *Nanoscale*, 2016, **8**, 11385–11391.

82 S. Venkateshalu and A. N. Grace, in *Fundamental Aspects and Perspectives of MXenes*, Springer, 2022, pp. 17–36, DOI: **10.1007/978-3-031-05006-0_2**.

83 M. Naguib, M. Kurtoglu, V. Presser, J. Lu, J. Niu, M. Heon, L. Hultman, Y. Gogotsi and M. W. Barsoum, *Adv. Mater.*, 2011, **23**, 4248–4253.

84 X. Li, Y. Bai, X. Shi, N. Su, G. Nie, R. Zhang, H. Nie and L. Ye, *Mater. Adv.*, 2021, **2**, 1570–1594.

85 J. Halim, M. R. Lukatskaya, K. M. Cook, C. R. Smith, L.-A. Näslund, S. J. May, L. Hultman, Y. Gogotsi, P. Eklund and M. W. Barsoum, *Chem. Mater.*, 2014, **26**, 2374–2381.

86 C. Xu, L. Wang, Z. Liu, L. Chen, J. Guo, N. Kang, X.-L. Ma, H.-M. Cheng and W. Ren, *Nat. Mater.*, 2015, **14**, 1135–1141.

87 J. Jeon, Y. Park, S. Choi, J. Lee, S. S. Lim, B. H. Lee, Y. J. Song, J. H. Cho, Y. H. Jang and S. Lee, *ACS Nano*, 2018, **12**, 338–346.

88 S. Zada, W. Dai, Z. Kai, H. Lu, X. Meng, Y. Zhang, Y. Cheng, F. Yan, P. Fu, X. Zhang and H. Dong, *Angew. Chem., Int. Ed.*, 2020, **59**, 6601–6606.

89 T. Li, L. Yao, Q. Liu, J. Gu, R. Luo, J. Li, X. Yan, W. Wang, P. Liu, B. Chen, W. Zhang, W. Abbas, R. Naz and D. Zhang, *Angew. Chem., Int. Ed.*, 2018, **57**, 6115–6119.

90 J. Mei, G. A. Ayoko, C. Hu, J. M. Bell and Z. Sun, *Sustainable Mater. Technol.*, 2020, **25**, e00156.

91 Y. Li, H. Shao, Z. Lin, J. Lu, L. Liu, B. Duployer, P. O. Å. Persson, P. Eklund, L. Hultman, M. Li, K. Chen, X.-H. Zha, S. Du, P. Rozier, Z. Chai, E. Raymundo-Piñero, P.-L. Taberna, P. Simon and Q. Huang, *Nat. Mater.*, 2020, **19**, 894–899.

92 H. Shi, P. Zhang, Z. Liu, S. Park, M. R. Lohe, Y. Wu, A. Shaygan Nia, S. Yang and X. Feng, *Angew. Chem., Int. Ed.*, 2021, **60**, 8689–8693.

93 J. Wang, S. Liu, Y. Wang, T. Wang, S. Shang and W. Ren, *J. Mater. Chem. C*, 2020, **8**, 1608–1613.

94 P. Horak, J. Vacik, S. Bakardjieva, A. Cannavo, G. Ceccio, J. Kupcik and R. Klie, *Microsc. Microanal.*, 2019, **25**, 1626–1627.

95 P. Urbankowski, B. Anasori, K. Hantanasirisakul, L. Yang, L. Zhang, B. Haines, S. J. May, S. J. L. Billinge and Y. Gogotsi, *Nanoscale*, 2017, **9**, 17722–17730.

96 P. Jeevanandam, Y. Koltypin, A. Gedanken and Y. Mastai, *J. Mater. Chem.*, 2000, **10**, 511–514.

97 M. Rajamathi, P. V. Kamath and R. Seshadri, *Mater. Res. Bull.*, 2000, **35**, 271–278.

98 L. Poul, N. Jouini and F. Fiévet, *Chem. Mater.*, 2000, **12**, 3123–3132.

99 J. Wu, R. Mi, S. Li, P. Guo, J. Mei, H. Liu, W.-M. Lau and L.-M. Liu, *RSC Adv.*, 2015, **5**, 25304–25311.

100 G. M. Tomboc, J. Kim, Y. Wang, Y. Son, J. Li, J. Y. Kim and K. Lee, *J. Mater. Chem. A*, 2021, **9**, 4528–4557.

101 A. I. Khan and D. O'Hare, *J. Mater. Chem.*, 2002, **12**, 3191–3198.

102 C. Wang, X. Zhang, Z. Xu, X. Sun and Y. Ma, *ACS Appl. Mater. Interfaces*, 2015, **7**, 19601–19610.

103 J. Y. Chen, L. Dang, H. Liang, W. Bi, J. B. Gerken, S. Jin, E. E. Alp and S. S. Stahl, *J. Am. Chem. Soc.*, 2015, **137**, 15090–15093.

104 D. Basu, A. Das, K. W. Stöckelhuber, U. Wagenknecht and G. Heinrich, *Prog. Polym. Sci.*, 2014, **39**, 594–626.

105 V. Rives, M. Del Arco and C. Martín, *J. Controlled Release*, 2013, **169**, 28–39.

106 G. Mascolo, *Appl. Clay Sci.*, 1995, **10**, 21–30.

107 M. Richetta, P. Medaglia, A. Mattoccia, A. Varone and R. Pizzoferrato, *J. Mater. Sci. Eng.*, 2017, **6**, 360.

108 M. Tabish, G. Yasin, M. J. Anjum, M. U. Malik, J. Zhao, Q. Yang, S. Manzoor, H. Murtaza and W. Q. Khan, *J. Mater. Res. Technol.*, 2021, **10**, 390–421.

109 L. Guo, W. Wu, Y. Zhou, F. Zhang, R. Zeng and J. Zeng, *J. Mater. Sci. Technol.*, 2018, **34**, 1455–1466.

110 Z. P. Xu and G. Q. Lu, *Chem. Mater.*, 2005, **17**, 1055–1062.

111 J. Prince, A. Montoya, G. Ferrat and J. S. Valente, *Chem. Mater.*, 2009, **21**, 5826–5835.

This journal is © The Royal Society of Chemistry 2023

J. Mater. Chem. A, 2023, **11**, 14469–14488 | **14487**

112 Z. Liu, R. Ma, M. Osada, N. Iyi, Y. Ebina, K. Takada and T. Sasaki, *J. Am. Chem. Soc.*, 2006, **128**, 4872–4880.

113 C. Prasad, X. Yang, Q. Liu, H. Tang, A. Rammohan, S. Zulfiqar, G. V. Zyryanov and S. Shah, *J. Ind. Eng. Chem.*, 2020, **85**, 1–33.

114 R. Yang, X. Chen, W. Ke and X. Wu, *Nanomaterials*, 2022, **12**, 1907.

115 Y. Ma, D. Xu, W. Chen, Y. Tang, X. Wang, L. Li and J. Wang, *Appl. Surf. Sci.*, 2022, **572**, 151432.

116 X. B. Joseph, J. N. Baby, S.-F. Wang, B. Sriram and M. George, *ACS Sustainable Chem. Eng.*, 2021, **9**, 14900–14910.

117 J. Pan, S. Li, L. Zhang, F. Li, Z. Zhang, T. Yu and D. Zhang, *J. Energy Storage*, 2022, **55**, 105415.

118 C. Hao, Y. Wu, Y. An, B. Cui, J. Lin, X. Li, D. Wang, M. Jiang, Z. Cheng and S. Hu, *Mater. Today Energy*, 2019, **12**, 453–462.

119 M. Cai, X. Fan, H. Yan, Y. Li, S. Song, W. Li, H. Li, Z. Lu and M. Zhu, *Chem. Eng. J.*, 2021, **419**, 130050.

120 C. Sun, P. Zuo, W. Sun, R. Xia, Z. Dong, L. Zhu, J. Lv, G. Deng, L. Tan and Y. Dai, *ACS Appl. Energy Mater.*, 2020, **3**, 10242–10254.

121 X. Feng, Z. Yu, R. Long, X. Li, L. Shao, H. Zeng, G. Zeng and Y. Zuo, *Sep. Purif. Technol.*, 2020, **253**, 117525.

122 Y. Wang, F. Xu, F. Zhou, L. Dai, K. Qu, Y. Wu, S. Gu and Z. Xu, *Ind. Eng. Chem. Res.*, 2022, **61**, 8800–8808.

123 D. W. Hobson, in *Comprehensive Biotechnology*, ed. M. Moo-Young, Academic Press, Burlington, 2nd edn, 2011, pp. 683–697, DOI: 10.1016/B978-0-08-088504-9.00228-2.

124 G. M. Whitesides and M. Boncheva, *Proc. Natl. Acad. Sci. U. S. A.*, 2002, **99**, 4769–4774.

125 A. M. Kalsin, M. Fialkowski, M. Paszewski, S. K. Smoukov, K. J. Bishop and B. A. Grzybowski, *Science*, 2006, **312**, 420–424.

126 E. B. Lindgren, I. N. Derbenev, A. Khachatourian, H.-K. Chan, A. J. Stace and E. Besley, *J. Chem. Theory Comput.*, 2018, **14**, 905–915.

127 C. Feng, Z. Zhao, C. Luo, Y. Wang, X. Wu and W. Chen, *Ceram. Int.*, 2022, **48**, 3884–3894.

128 X. Wu, B. Huang, Q. Wang and Y. Wang, *Chem. Eng. J.*, 2020, **380**, 122456.

129 Y. Zhang, J. Cao, J. Li, Z. Yuan, D. Li, L. Wang and W. Han, *Chem. Eng. J.*, 2022, **430**, 132992.

130 Z. Yan, H. Sun, X. Chen, H. Liu, Y. Zhao, H. Li, W. Xie, F. Cheng and J. Chen, *Nat. Commun.*, 2018, **9**, 2373.

131 M. Datta and D. Landolt, *Electrochim. Acta*, 2000, **45**, 2535–2558.

132 S. Saha and S. Das, in *Chemical Solution Synthesis for Materials Design and Thin Film Device Applications*, Elsevier, 2021, pp. 561–583, DOI: 10.1016/b978-0-12-819718-9.00017-0.

133 N. Labchir, A. Hannour, D. Vincent, A. Ihlal and M. Sajieddine, *Curr. Appl. Phys.*, 2021, **25**, 33–40.

134 C. Wang, Y. Zhong, W. Ren, Z. Lei, Z. Ren, J. Jia and A. Jiang, *Appl. Surf. Sci.*, 2008, **254**, 5649–5654.

135 L. Hu, M. Li, X. Wei, H. Wang, Y. Wu, J. Wen, W. Gu and C. Zhu, *Chem. Eng. J.*, 2020, **398**, 125605.

136 J. Wang, X. Wei, W. Song, X. Shi, X. Wang, W. Zhong, M. Wang, J. Ju and Y. Tang, *ChemSusChem*, 2021, **14**, 1948–1954.

137 H. Li, S. Lin, H. Li, Z. Wu, Q. Chen, L. Zhu, C. Li, X. Zhu and Y. Sun, *Small Methods*, 2022, **6**, 2101320.

138 R. Zhang, J. Dong, W. Zhang, L. Ma, Z. Jiang, J. Wang and Y. Huang, *Nano Energy*, 2022, **91**, 106633.

139 R. Zhang, Z. Xue, J. Qin, M. Sawangphruk, X. Zhang and R. Liu, *J. Energy Chem.*, 2020, **50**, 143–153.

140 Y. Liu, L. Bai, T. Li, H. Liu, X. Wang, L. Zhang, X. Hao, C. He and S. Guo, *Mater. Adv.*, 2022, **3**, 4359–4368.

141 X.-D. Zhu, Y. Xie and Y.-T. Liu, *J. Mater. Chem. A*, 2018, **6**, 21255–21260.

142 Q. Xiang, F. Li, W. Chen, Y. Ma, Y. Wu, X. Gu, Y. Qin, P. Tao, C. Song and W. Shang, *ACS Energy Lett.*, 2018, **3**, 2357–2365.

143 Z. Bai, D. Zhang, Y. Guo, Y. Yang, H. Yan, Y. Wang, J. Cheng, P. K. Chu, H. Pang and Y. Luo, *Adv. Sustainable Syst.*, 2022, **6**, 2100371.

144 X. Jin, H. Piao, Y. Sun, J.-H. Choy and S.-J. Hwang, *2D Mater.*, 2022, **9**, 044005.

145 X. Wang, H. Li, H. Li, S. Lin, J. Bai, J. Dai, C. Liang, X. Zhu, Y. Sun and S. Dou, *J. Mater. Chem. A*, 2019, **7**, 2291–2300.

146 C. Li, Z. Dai, W. Liu, P. Kantichaimongkol, P. Yu, P. Pattananuwat, J. Qin and X. Zhang, *Chem. Comm.*, 2021, **57**, 11378–11381.

147 H. Li, Y. Wen, X. Zhu, J. Wang, L. Zhang and B. Sun, *ACS Sustainable Chem. Eng.*, 2019, **8**, 520–526.

148 Z. Zhao, X. Wu, C. Luo, Y. Wang and W. Chen, *J. Colloid Interface Sci.*, 2022, **609**, 393–402.

149 F. Liu, C. Wang, L. Wang, F. Huang, J. Fan, N. Shi, M. Han and Z. Dai, *ACS Appl. Energy Mater.*, 2022, **5**, 3346–3358.

150 X. Kan, J.-C. Wang, Z. Chen, J.-Q. Du, J.-L. Kan, W.-Y. Li and Y.-B. Dong, *J. Am. Chem. Soc.*, 2022, **144**, 6681–6686.

151 R. Zhao, M. Wang, D. Zhao, H. Li, C. Wang and L. Yin, *ACS Energy Lett.*, 2017, **3**, 132–140.

152 C. Li, D. Zhang, J. Cao, P. Yu, M. Okhawilai, J. Yi, J. Qin and X. Zhang, *ACS Appl. Energy Mater.*, 2021, **4**, 7821–7828.

153 L. Song, S. Zhu, L. Tong, W. Wang, C. Ouyang, F. Xu and Y. Wang, *Mater. Adv.*, 2021, **2**, 5622–5628.

154 D. Zhang, J. Cao, X. Zhang, N. Insin, S. Wang, Y. Zhao and J. Qin, *ACS Appl. Energy Mater.*, 2020, **3**, 11119–11130.

155 J. Shen, G. Yang, G. Duan, X. Guo, L. Li and B. Cao, *Dalton Trans.*, 2022, **51**, 18462–18472.

156 M. Benchakar, T. Bilyk, C. Garnero, L. Loupias, C. Morais, J. Pacaud, C. Canaff, P. Chartier, S. Morisset and N. Guignard, *Adv. Mater. Interfaces*, 2019, **6**, 1901328.

157 M. Tian, Y. Jiang, H. Tong, Y. Xu and L. Xia, *ChemNanoMat*, 2020, **6**, 154–159.

158 M. Xia, M. Yang, Y. Guo, X. Sun, S. Wang, Y. Feng and H. Ding, *ChemNanoMat*, 2022, **8**, e202200113.

159 J. Lei, Y. Xiong, F. Yu and J. Ma, *Chem. Eng. J.*, 2022, **437**, 135381.

160 Y. Zhou, F. Chu, L. Ding, W. Yang, S. Zhang, Z. Xu, S. Qiu and W. Hu, *Chemosphere*, 2022, **297**, 134134.

161 A. Grzegórska, J. Wysocka, P. Głuchowski, J. Ryl, J. Karczewski and A. Zielińska-Jurek, *Chemosphere*, 2022, **308**, 136191.

162 Z. Zhao, X. Wu, C. Luo, Y. Wang and W. Chen, *J. Colloid Interface Sci.*, 2022, **609**, 393–402.

14488 | *J. Mater. Chem. A*, 2023, **11**, 14469–14488

This journal is © The Royal Society of Chemistry 2023